We are IntechOpen, the world's leading publisher of Open Access books Built by scientists, for scientists

4,800
Open access books available

122,000
International authors and editors

135M
Downloads

Our authors are among the

154
Countries delivered to

TOP 1%
most cited scientists

12.2%
Contributors from top 500 universities

WEB OF SCIENCE™

Selection of our books indexed in the Book Citation Index in Web of Science™ Core Collection (BKCI)

Interested in publishing with us?
Contact book.department@intechopen.com

Numbers displayed above are based on latest data collected.
For more information visit www.intechopen.com

10

Photonics Crystal Fiber Loop Mirrors and Their Applications

Chun-Liu Zhao[1], Xinyong Dong[1], H. Y. Fu[2] and H. Y. Tam[2]
[1]*Institute of Optoelectronic Technology, China Jiliang University, Hangzhou*
[2]*Photonics Research Centre, Department of Electrical Engineering, The Hong Kong Polytechnic University, Hung Hom, Kowloon, Hong Kong SAR*
China

1. Introduction

Fiber loop mirrors (FLMs), also called Sagnac interferometers, are interesting and very useful components for use in optical devices and systems [1, 2]. Many components based on FLMs have been demonstrated for applications in wavelength-division-multiplexing filters and in sensors, among others [3-7]. In FLM, the two interfering waves counter-propagate through the same fiber and are exposed to the same environment. This makes it less sensitive to noise from the environment. In general, a conventional fiber loop mirror made of high-birefringent fibers (HiBi fibers) or polarization-maintaining fibers (PMFs) has several advantages compared with a Mach–Zehnder interferometer, such as insensitivity, high extinction ratio, in-dependence of input polarization, easy to manufacture and low cost [1, 2]. However, conventional PMFs (e.g., Panda and bow-tie PMFs) have a high thermal sensitivity due to the large thermal expansion coefficient difference between boron-doped stress-applying parts and the cladding (normally pure silica). Consequently, conventional PMFs exhibit temperature-sensitive birefringence [8]. Therefore, conventional PMF based Sagnac interferometers exhibit relatively high temperature sensitivity, which is about 1 and 2 orders of magnitude higher than that of long-period fiber grating (LPG) and fiber Bragg grating (FBG) sensors [9, 10]. This can limit the practical use of the devices in some applications.

Various kinds of sensors based on HiBi-FLMs have been proposed and realized since HiBi-FLMs are sensitive to many parameters and have a high sensitivity, such as temperature sensors, level liquid sensors, refractive index sensors, strain sensors and biochemical sensors [7, 9-12]. However, when a HiBi-FLM is used to measure strain or other parameters, its cross-sensitivity to temperature may degrade sensor performance since the optical path length of the HiBi-FLM shows temperature dependence caused by thermal refractive-index change and thermal expansion effect. Thus, the temperature effect must be discriminated or eliminated when they are used for sensing [13-15].

The photonic crystal fiber (PCF) is a new class of optical fiber that emerged in recent years. Typically, these fibers incorporate a number of air holes that run along the length of the fiber and have a variety of different shapes, sizes, and distributions [16-17]. Of the many unusual properties exhibited by a PCF, a particularly exciting feature is that the PCF can be made HiBi by arranging the core and the air-hole cladding geometry, thereby introducing

asymmetry [18-19]. Their birefringence can be of the order of 10^{-3}, which is about one order of magnitude larger than that of conventional HiBi fibers. Unlike conventional PMFs (bow-tie, elliptical core, or Panda), which contain at least two different glasses each with a different thermal expansion coefficient, thereby causing the polarization of the propagation wave to vary with changing temperature, the PCF birefringence is highly insensitive to temperature because it is made of only one material (and air holes). Recently, some of FLMs used PCFs have been developed and applied on various devices [20-22] and optical fiber sensors [24-35], including strain sensors, pressure sensors, temperature sensors and curvature sensors, and so on.

In this chapter, we will first introduce the basic operation principle of FLMs, secondly, will demonstrate a temperature-insensitive interferometer based on a HiBi-PCF FLM. We will then move on to various applications in optical sensors such as strain sensors, pressure sensors, and temperature sensors. Following, we will discuss a demodulation technology of HiBi-PCF FLM based sensors. Finally, we will describe several multiplexing schemes for HiBi-PCF based FLM sensors.

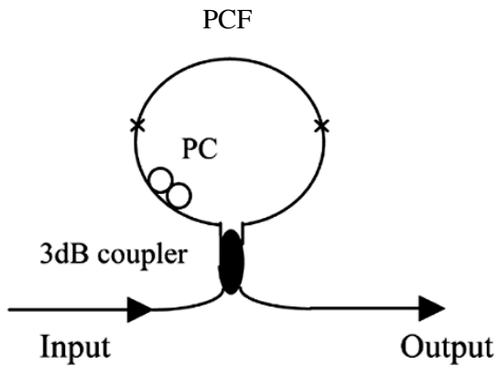

Fig. 1. Configuration of FLM made of a PCF.

2. Basic principle of FLMs

As shown in Fig. 1, the 3-dB coupler splits the input signal equally into two counter-propagating waves which subsequently recombine (at the coupler) after propagating around the loop. The interference of the counter-propagating waves will be constructive or destructive, depending on the birefringence of the cavity, and thus, the loop transmission response is wavelength dependent. The phase difference between the fast and slow beams that propagate in the PCF is given by [1, 2]:

$$\theta = 2\pi BL / \lambda \tag{1}$$

where B, L, and λ are the birefringence of the PCF, the length of the PCF and the wavelength, respectively. When the variation of B following the wavelength is small, there is $B=/n_x-n_y/$, where n_x and n_y are the effective refractive index for each polarization mode. Ignoring insertion loss of the 3-dB coupler and the attenuation of the PCF and the single-mode fiber in the loop, the transmission spectrum of the fiber loop is approximately a periodic function of the wavelength, namely,

$$T = (1 - \cos\theta) / 2 \tag{2}$$

The transmission dip wavelengths are the resonant wavelengths satisfying $2\pi BL/\lambda_{dip} = 2k\pi$, where k is any integer. Thus, the resonant dip wavelengths can be described as

$$\lambda_{dip} = BL / k \tag{3}$$

And the wavelength spacing between transmission dips can be expressed as

$$S = \lambda^2 / BL \tag{4}$$

When some varies (strain or temperature) applied on the PCF sensing element, they will cause the birefringence change ΔB and length change ΔL of the PCF. So the λ_{dip} has a change and it can be expressed as:

$$\Delta\lambda_{dip} = (\Delta BL + B\Delta L) / k \tag{5}$$

So the change of varies can be obtained by measuring the wavelength shift of the dip in the output spectrum. The setting of the polarization controller (PC) can affect the contrast of the transmission function. By adjusting the state of the PC, transmission bands with large extinction ratio can be obtained.

3. Temperature-insensitive interferometer using a HiBi-PCF FLM [21]

In general, the optical path length of a conventional HiBi-FLM shows temperature dependence caused by thermal refractive-index change and thermal expansion of the devices [8]. This can limit the practical use of the device. In this part, utilizing the high birefringence and the low temperature coefficient of birefringence, a temperature-insensitive interferometer based on a HiBi-PCF FLM is realized.

In this experiment, a 6.5-cm-long HiBi-PCF was used, which was fabricated by Blaze-Photonics Com., and the cross-sectional scanning electron micrograph is shown in Fig. 2. Mode field diameters at the two orthogonal polarizations are 3.6 and 3.1 μm. The HiBi-PCF has a group birefringence Δn_g of 8.65×10^{-4} at 1550 nm, and a nominal beat length of 1.8 mm. Both ends of the HiBi-PCF are spliced to conventional single-mode fiber (SMF) by using a CO_2 laser splicing system. The PCF-SMF splicing loss is large (about 3.5 dB) because of mismatching of mode field and numerical apertures between the PCF and the SMF. The splicing loss will be reduced when a pre-tapering technology is used. The PCF-SMF splicing losses will increase the total insertion loss of the HiBi-PCF-FLM. The device characteristics are measured with a tunable laser source (Agilent 81689 A) which can be tuned from 1.5 to 1.6 μm and a power sensor (Agilent 81634 A).

Fig. 3 shows the transmission spectra of the HiBi-PCF-FLM at different temperatures. The temperature of the HiBi-PCF-FLM is controlled by a temperature chamber during measurement. The transmission spectrum is approximately a periodic function of wavelength, as given by equation (2). The corresponding wavelength spacing between transmission peaks is about 0.43 nm, which is consistent with equation (4). The extinction ratio is nearly 26 dB and the total insertion loss of the HiBi-PCF-FLM is 10 dB.

Since the phase difference is given by equation (1), a change of the phase matching condition caused by the environment leads to a wavelength spacing variation and a resonance wavelength shift. As shown in Fig. 3 and Fig. 4, when the ambient temperature of the HiBi-PCF-FLM is increased, the transmission peaks shift a little to shorter wavelength. We choose

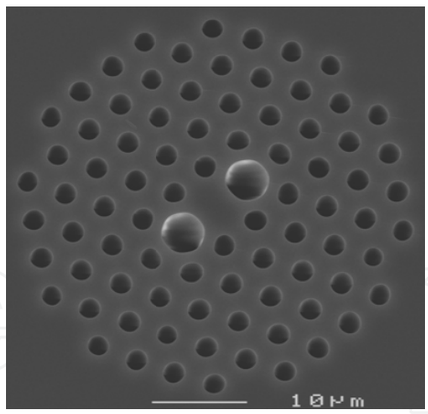

Fig. 2. Scanning electron micrograph of the cross section of the HiBi-PCF.

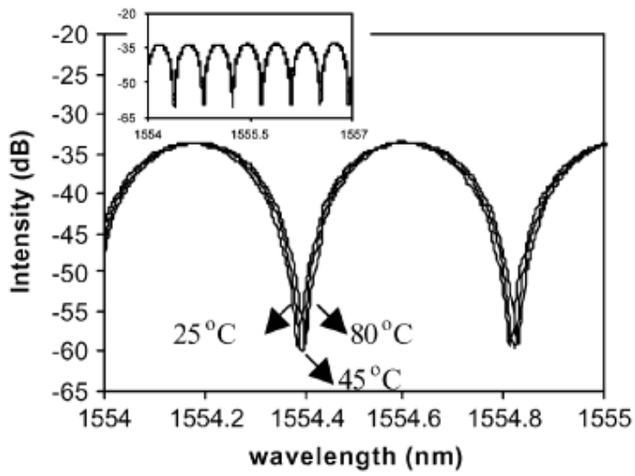

Fig. 3. Transmission spectra as a function of temperature for the HiBi-PCF-FLM, insertion: the transmission spectra in the range of 1554 -1557 nm.

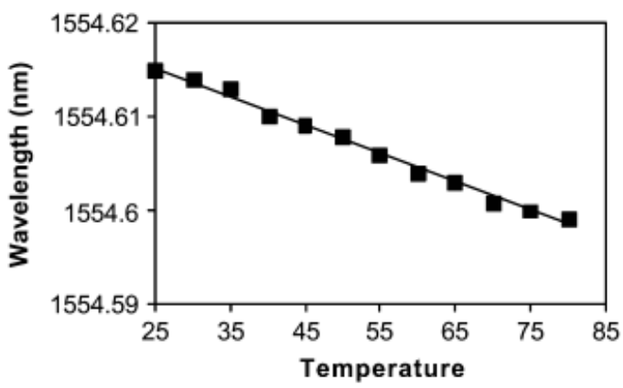

Fig. 4. Variation of the transmission peak wavelength at 1554.6 nm with temperature for the HiBi-PCF-FLM.

the transmission peak at 1554.6 nm as an example. The wavelength shift of the transmission peak with temperature is 0.3 pm /°C. The line (a) in Fig. 5, which is for the HiBi-PCF-FLM, shows the wavelength spacing change with temperature. The variation of wavelength spacing is very small: only 0.05 pm /°C.

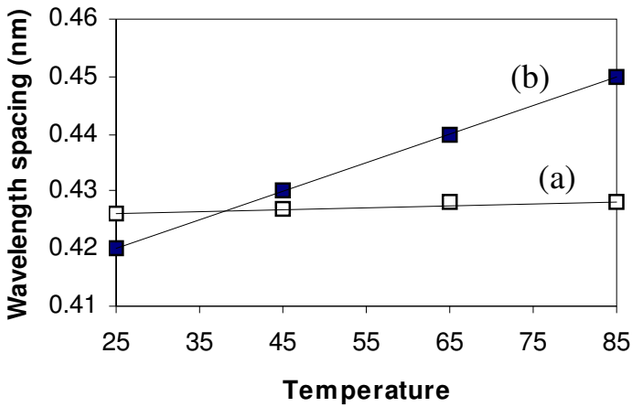

Fig. 5. Variation of the wavelength spacing with temperature (a) the HiBi-PCF-FLM; (b) the PMF-FLM.

In order to compare the new HiBi-PCF-FLM with the conventional FLM, we used a Panda polarization maintaining fiber (PMF) as the HiBi fiber. The Panda PMF is from Fujikura (SM-13P) with a measured birefringence of Δn_g = 3.85×10-4 at 1550 nm. The length of the Panda PMF is about 14.8 m. The wavelength spacing of the PMF-FLM is about 0.42 nm at temperature 25 °C. The extinction ratio is about 25 dB. As shown in Fig. 6, the transmission peaks shift very significantly at different temperatures. The line (b) in Fig. 5 shows the temperature dependence of the wavelength spacing for the conventional PMF-FLM. The variation of the wavelength spacing with temperature is about 0.5 pm /°C, which is nearly

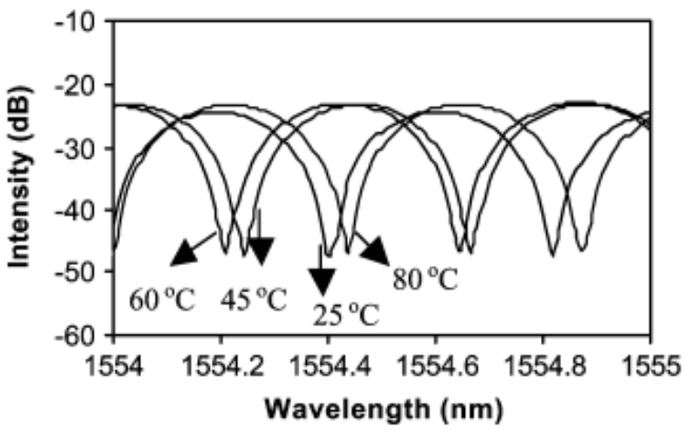

Fig. 6. Transmission spectra for the HiBi-PMF-FLM at different temperatures.

ten times of that for the HiBi-PCF-FLM. Furthermore, Fig. 7 shows the transmission peak shift as a function of temperature for the PMF-FLM. In theory, the wavelength shift of transmission peaks with temperature is nearly 16.6 pm /°C. In the experiment, however, the polarization of the propagation wave may vary with temperature, because different glasses of the PMF have different thermal expansion coefficient. This also effects the stability of the PMF-FLM. Such a large variation of the properties of the FLM made of conventional PMF with temperature makes it unsuitable for many applications in optical communication or sensor systems. However, by using HiBi-PCF, temperature-insensitivity of the FLM is improved by about 55 times.

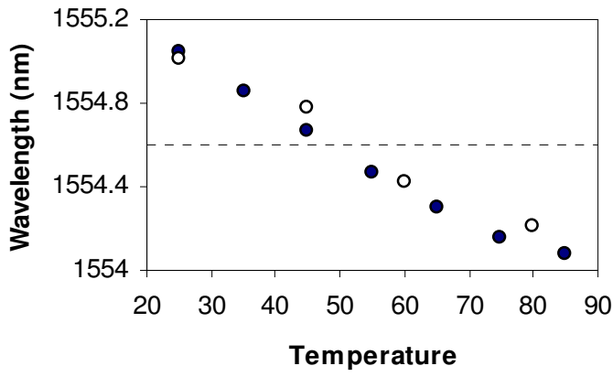

Fig. 7. Variation of the transmission peak wavelength near 1554.6 nm with temperature for the HiBi-PMF-FLM (●: theoretical and ○: experimental results).

4. Optical fiber sensors based on a HiBi-PCF FLM

4.1 A temperature independent strain sensor based on a HiBi-PCF FLM [24]

Strain sensors based on the strain-induced variation in birefringence of the HiBi fibers used in FLMs were also proposed and characterized. These sensors possess lots of advantages including simple design, easy to manufacture, high sensitivity, and low cost. However, previously reported FLM sensors are all based on conventional HiBi fibers whose birefringence is dependent on temperature. When they are used for sensing other measurands such as strain, the high thermal response of conventional PMFs may cause serious cross-sensitivity effects and reduce the measurement accuracy. In this part, a HiBi-PCF FLM strain sensor is demonstrated. The strain measurement is inherently temperature insensitive due to the great thermal stability of HiBi-PCF based FLM.

The proposed FLM strain sensor is as shown in Fig.8. When a strain is applied on the HiBi-PCF, the phase change induced by an elongation ΔL (i.e., a strain $\varepsilon = \Delta L / L$) to the PM-PCF can be given approximately by

$$\Delta\theta = \frac{2\pi}{\lambda}[\Delta LB + L\Delta B] \tag{6}$$

where $\Delta B = \triangle n_x - \triangle n_y$, is the variation of birefringence of the PM-PCF caused by photoelastic effect. Based on the analysis of photoelastic effect in single-mode fibers [35], the change of effective refractive index in the fiber core is related to the applied strain with a coefficient

named effective photoelastic constant. It is therefore assumed that $\triangle n_x$ and $\triangle n_y$ have similar descriptions but different effective photoelastic constants, expressed as follows:

$$\Delta n_x = p_e^x n_x \varepsilon \text{ , and} \tag{7a}$$

$$\Delta n_y = p_e^y n_y \varepsilon \tag{7b}$$

Where p_e^x and p_e^y are the effective photoelastic constant for the slow and fast axes, respectively. By substituting Eqs. (7a) and (7b) into Eq.(6) and considering the relationship between spectrum (or peak wavelength) shift and phase change, i.e., $\Delta\lambda = S\Delta\theta/(2\pi)$, the following relationship can be obtained:

$$\Delta\lambda = \lambda(1 + p_e')\varepsilon \tag{8}$$

where $P_e' = (n_y p_e^y - n_x p_e^x)/B$, is a constant that describes the strain-induced variation of the birefringence of the PM-PCF.

From Eq. (8), it can be seen that $\Delta\lambda$ is directly proportional to ε; therefore, linear spectrum (or peak wavelength) shift is expected with change of the applied strain.

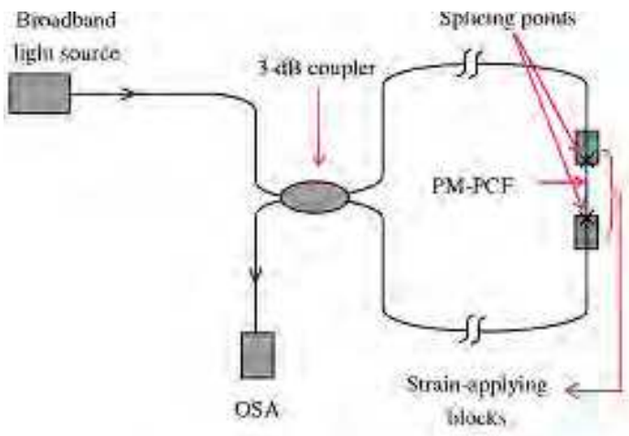

Fig. 8. Experimental setup of the proposed strain sensor based on a FLM made of a highly birefringent PCF.

In the experiment, the HiBi-PCF is 86 mm long, whose structure is the same as that in the section 3. Fig. 9 shows the transmission spectrum of the HiBi-PCF based FLM within a wide wavelength range of 70 nm. The wavelength spacing between the two transmission minima is 32.5 nm, and a good extinction ratio of 32 dB was achieved at the first transmission minimum located at 1547 nm. Since the light source we used is not polarized and there is no polarization-dependent element used in the sensor system, the stability of the sensor output against environmental variations, such as small vibrations, is good.

We fixed one end of the HiBi-PCF and stretched the other end by using a precision translation stage. Fig. 10 shows several measured transmission spectra around the transmission minimum at 1547 nm under different applied strains. The spectrum shifted 7.5 nm to the longer wavelength direction when the strain was increased from 0 to 32 m. The measured data are shown in Fig.11. A linear fitting to the experimental data gives a

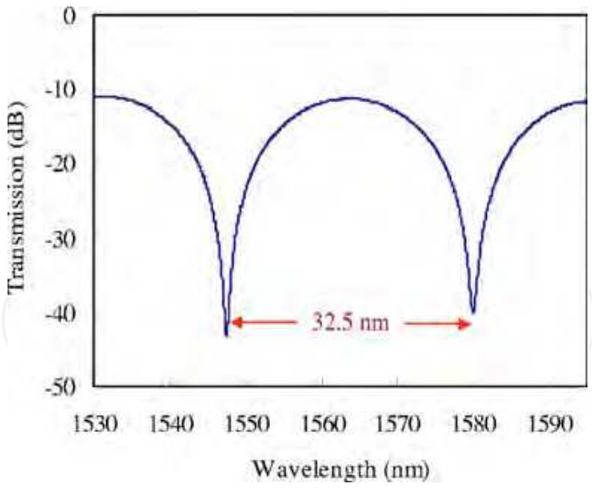

Fig. 9. The transmission spectrum of the HiBi-PCF FLM.

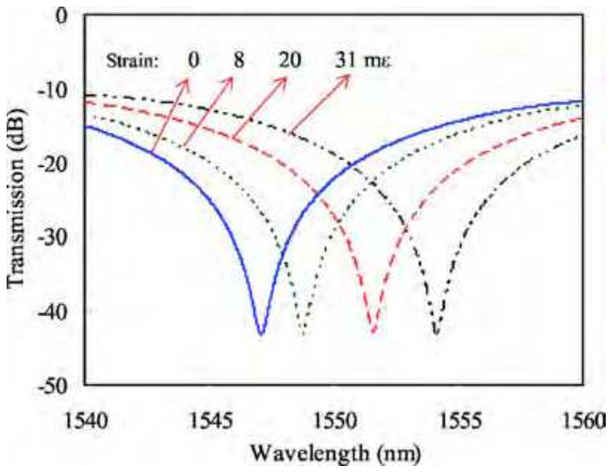

Fig. 10. Measured transmission spectra under different strains.

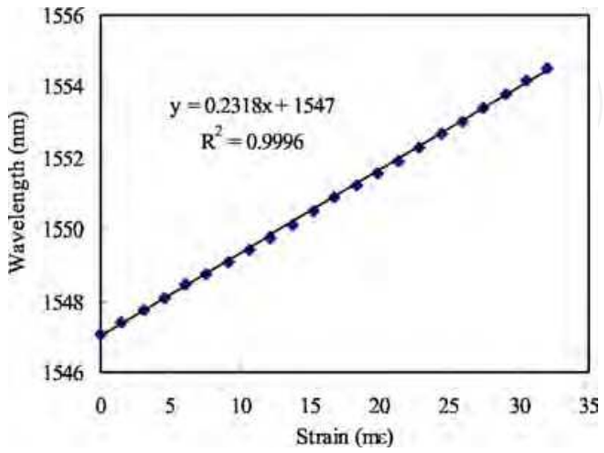

Fig. 11. Wavelength shift of the transmission minimum at 1547 nm against the applied strain.

wavelength-strain sensitivity of 0.23 pm/$\mu\varepsilon$ and a high R^2 value of 0.9996, which shows that the linearity of the wavelength to strain response is excellent. Therefore, the experimental data agree well with the theoretical prediction, and the constant p_e' in Eq. (8), calculated from the wavelength-strain sensitivity value, is -0.82.

The resolution of the strain measurement, limited by the 10 pm wavelength resolution of the used OSA, is 43 $\mu\varepsilon$, which is actually quite high when taking into account the large measurement range. The maximum value of the applied strain is mostly determined by the maximum strain that the HiBi-PCF can endure, not the strength of the fusion splicing points because the two splicing points between the HiBi-PCF and SMFs were prevented from being stretched as they were glued to the strain-applying blocks. As a result, the measurement range is several times larger than that of fiber Bragg grating and long-period grating sensors, where the fiber strength is significantly weaken during the grating inscription by high power ultraviolet laser beams [37]. This may be regarded as one of the several advantages of the proposed HiBi-PCF based the strain sensor over the two kinds of fiber grating sensors.

Temperature stability of the HiBi-PCF FLM strain sensor was also tested by setting the sensor head into a temperature-controlled container. The transmission minimum at 1547 nm was moved to shorter wavelength by only 22 pm when the temperature was increased up to 80°C. Measurement results are shown in Fig.12. The temperature sensitivity is only 0.29 pm/°C, which, compared with the reported value of 0.99 nm/°C of the FLM temperature sensor based on conventional PMF [7], is about 3000 times lower. The temperature sensitivity is also in good agreement with the previously reported value in Ref. 21 where the same HiBi-PCF was used. If a temperature variation of 30°C is assumed, the corresponding wavelength shift of the strain sensor is only 8.7 pm, which is even smaller than the wavelength resolution of the OSA. Therefore, such a low temperature sensitivity can be totally neglected when the sensor is operated in normal environmental condition without very large temperature variations.

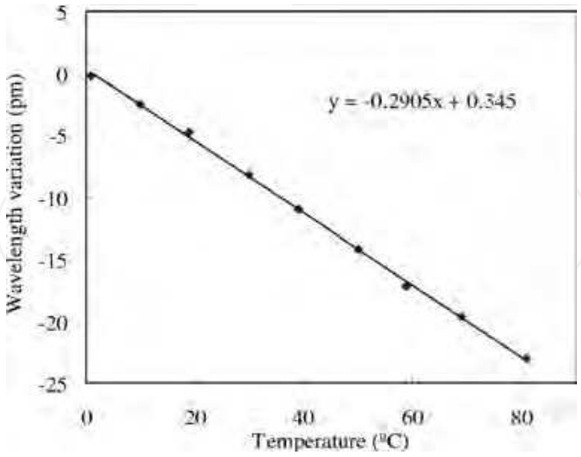

Fig. 12. Wavelength variation of the transmission minimum at 1547 nm against temperature.

Compared with the conventional HiBi fiber based FLM sensors and fiber Bragg grating or long-period grating sensors, the HiBi-PCF FLM strain sensor is inherently insensitive to temperature, eliminating the requirement for temperature compensation. It is also simple, easy to manufacture, potentially low cost, and possesses a much larger measurement range.

4.2 Pressure sensor realized with a HiBi-PCF FLM [29]

In this part, we demonstrate a pressure sensor based on a HiBi-PCF FLM. The FLM itself acts as a sensitive pressure sensing element, making it an ideal candidate for pressure sensor. Other reported fiber optic pressure sensors generally required some sort of modification to the fiber to increase their sensitivity [38]. The HiBi-PCF FLM pressure sensor does not require polarimetric detection and the pressure information is wavelength encoded.

Fig. 13 shows the experimental setup of the pressure sensor with the HiBi-PCF based FLM interferometer. The used HiBi-PCF is 58.4 cm and is laid in an open metal box and the box is placed inside a sealed air tank. The tank is connected to an air compressor with adjustable air pressure that was measured with a pressure meter. The input and output ends of the FLM are placed outside the air tank.

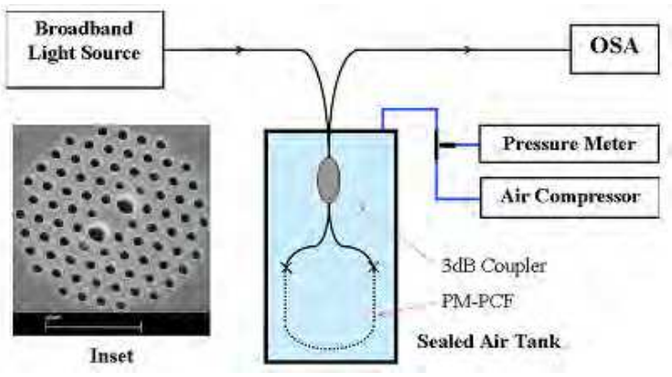

Fig. 13. The experimental setup of our proposed pressure sensor.

Ignoring the loss of the FLM, the transmission spectrum of the fiber loop is approximately a periodic function of the wavelength and is given as Eq. (1). The total phase difference θ introduced by the HiBi-PCF can be expressed as

$$\theta = \theta_0 + \theta_{\mathrm{p}} \tag{9}$$

where θ_0 and θ_P are the phase differences due to the intrinsic and pressure-induced birefringence over the length L of the HiBi-PCF and are given by

$$\theta_0 = \frac{2\pi \cdot B \cdot L}{\lambda} \tag{10}$$

$$\theta_{\mathrm{p}} = \frac{2\pi \cdot \left(\mathrm{K_p}\Delta \mathrm{p}\right) \cdot L}{\lambda} \tag{11}$$

ΔP is the applied pressure and the birefringence-pressure coefficient of HiBi-PCF can be described as [39]

$$K_P = \frac{\partial n_s}{\partial P} - \frac{\partial n_f}{\partial P}. \tag{12}$$

The pressure-induce wavelength shift of the transmission minimum is $\Delta\lambda = S \cdot \theta_P / 2\pi$. Thus the relationship between wavelength shift and applied pressure can be obtained as

$$\Delta\lambda = (\frac{K_P \cdot \lambda}{B}) \cdot \Delta P \,. \tag{13}$$

Eq. (13) shows that for a small wavelength shift, the spectral shift is linearly proportional to the applied pressure.

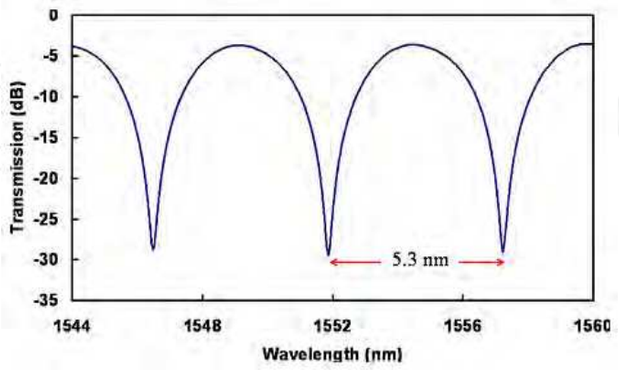

Fig. 14. Transmission spectrum of the HiBi-PCF based Sagnac interferometer.

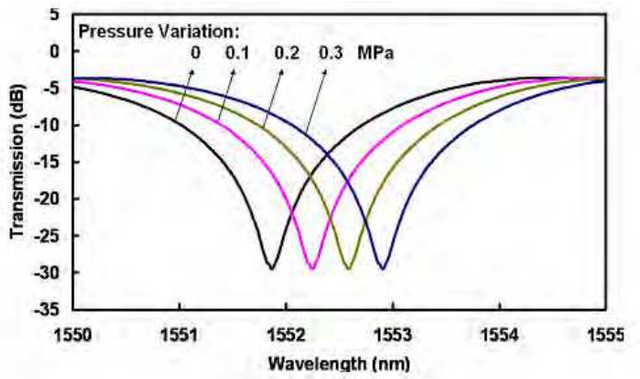

Fig. 15. Measured transmission spectra under different pressures.

Fig 14 shows the transmission spectrum of the HiBi-PCF FLM at atmospheric pressure, i.e., at zero applied pressure. The spacing between two adjacent transmission minimums is ~5.3 nm and an extinction ratio of better than 20 dB was achieved. The intrinsic birefringence of the HiBi-PCF used in our experiment is 7.8×10^{-4} at 1550 nm.

The air compressor is initially at one atmospheric pressure (about 0.1MPa). In the experiment, we can increase air pressure up to 0.3 MPa; thus, the maximum pressure that can be applied to the HiBi-PCF-based FLM sensor is ~0.4 MPa. At one atmospheric pressure one of the transmission minimums occurs at 1551.86 nm and shifts to a longer wavelength with applied pressure. When the applied pressure was increased by 0.3MPa, a 1.04 nm wavelength shift of the transmission minimum was measured, as shown in Fig 15. Fig. 16 shows the experimental data of the wavelength–pressure variation and the linear curve fitting. The measured wavelength–pressure coefficient is 3.42 nm/MPa with a good R^2 value of 0.999, which agrees well with the theoretical prediction. From Eq. (13), the birefringence–pressure coefficient is ~1.7×10^{-6} MPa^{-1}. The resolution of the pressure measurement is ~2.9 kPa when using an OSA with a 10 pm wavelength resolution. Because of the limitations of

our equipment, we have not studied the performance of this pressure sensor for high pressure at this stage. However, we found that the HiBi-PCF can stand pressure of 10 MPa without damage to its structure. This part of the work is ongoing and will be reported in our further studies.

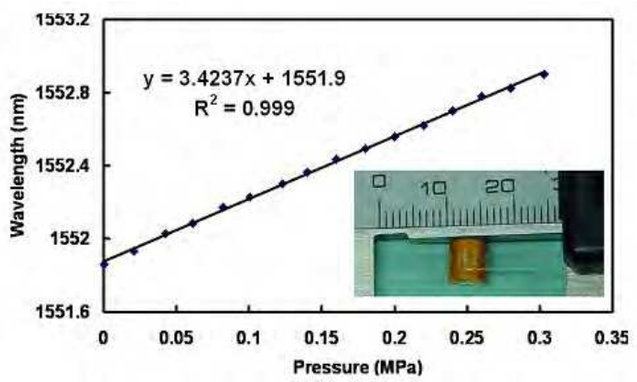

Fig. 16. Wavelength shift of the transmission minimum at 1551.86 nm against applied pressure with variation up to 0.3Mpa.

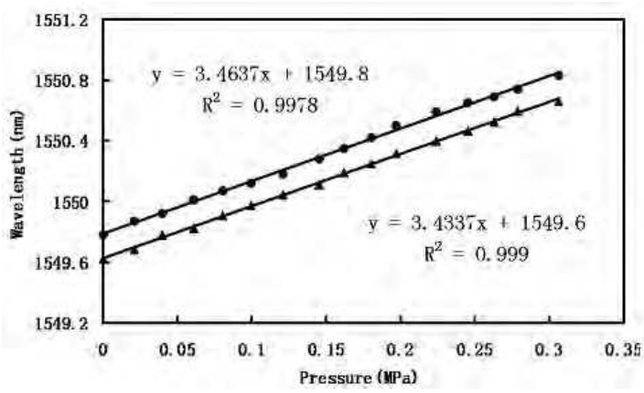

Fig. 17. Wavelength shift of the transmission minimum against applied pressure for HiBi-PCFs with length of 40 (circles) and 79.6 cm (triangles); the wavelength pressure coefficients are 3.46 and 3.43 nm/MPa, respectively.

Although the length of HiBi-PCF used in our experiment is 58.4 cm, it is important to note that the HiBi-PCF can be coiled into a very small diameter circle with virtually no additional bending loss so that a compact pressure sensor design can be achieved. The induced bending loss by coiling the HiBi-PCF into 10 turns of a 5mm diameter circle, shown in the inset of Fig. 16, is measured to be less than 0.01 dB with a power meter (FSM-8210, ILX Lightwave Corporation). The exceptionally low bending loss will simplify sensor design and packaging and fulfils the strict requirements of some applications where small size is needed, such as in down-hole oil well applications. To investigate the effects of coiling, we have studied two extreme cases in which the HiBi-PCF was wound with its fast axis and then its slow axis on the same plane of the coil. There were no measurable changes for either the birefringence or the wavelength–pressure coefficient when the fiber was coiled into 15 and 6mm diameter circles with both of the orientations coiling. The coiling of the HiBi-PCF

into small diameter circles makes the entire sensor very compact and could reduce any unwanted environmental distortions, such as vibrations.
The wavelength–pressure coefficient is independent of the length of the HiBi-PCF, as described in Eq. (13). Fig. 17 shows the wavelength-pressure coefficients are 3.46 and 3.43 nm/MPa for HiBi-PCFs with lengths of 40 and 79.6 cm, respectively. After comparing the two wavelength–pressure coefficients with that of the pressure sensor with a 58.4 cm HiBi-PCF (Fig. 17), we observed that the wavelength–pressure coefficient is constant around 1550 nm; this agrees well with our theoretical prediction. However, the length of the PM-PCF cannot be reduced too much because this would result in broad attenuation peaks in the transmission spectrum and that would reduce the reading accuracy of the transmission minimums.

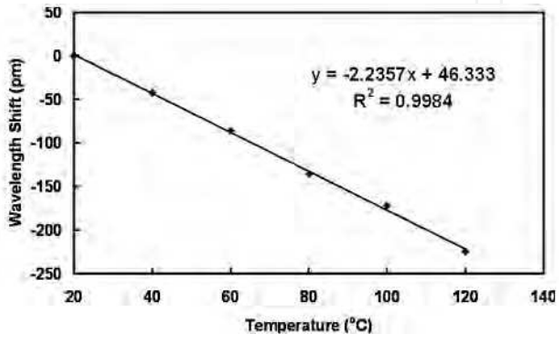

Fig. 18. Wavelength shift of the transmission minimum at 1551.86 nm against temperature.

Temperature sensitivity of the proposed pressure sensor is also investigated by placing the sensor into an oven and varying its temperature. Fig 18 shows the wavelength shift of a transmission minimum versus temperature linearly with a good R^2 value of 0.9984. The measured temperature coefficient is -2.2 pm/°C, which is much smaller than the 10 pm/°C of fiber Bragg grating. The temperature may be neglected for applications that operate over a normal temperature variation range.
Based on the small size, the high wavelength pressure coefficient, the reduced temperature sensitivity characteristic, and other intrinsic advantages of fiber optic sensors, such as light weight and electro-magnetically passive operation, the proposed pressure sensor is a promising candidate for pressure sensing even in harsh environments. Considering the whole pressure sensing system, we can also replace the light source with laser and use a photodiode for intensity detection at the sensing signal receiving end. Since the power fluctuation is very small even when the HiBi-PCF is bent, intensity detection is practical for real applications. Because of the compact size of the laser and photodiode, the entire system can be made into a very portable system. Furthermore, the use of intensity detection instead of wavelength measurement would greatly enhance interrogation speed and consequently makes the system much more attractive.

4.3 A high sensitive temperature sensor based on a FLM made of an alcohol-filled PCF [33]

HiBi-PCFs have a low thermo-optic and thermo-expansion coefficient HiBi-PCF, so HiBi-PCF FLMs can not be used to measure temperature directly. However, by inserting a short alcohol-filled HiBi-PCF into a FLM, a temperature sensor with an extremely high sensitivity can be realized by measuring the wavelength shift of the resonant dips of the alcohol-filled HiBi-PCF FLM.

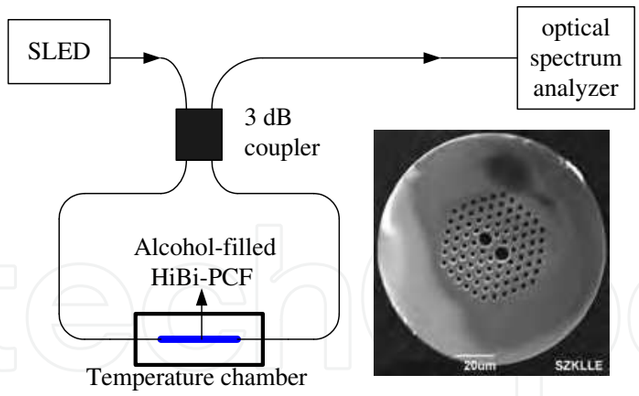

Fig. 19. Experimental setup of the temperature sensor based on a FLM inserted an alcohol-filled highly birefringent PCF. Insertion: SEM of the cross section of the used PCF.

The temperature sensor, as shown in Fig. 19, consists of a 3dB coupler and a short alcohol-filled PCF. Alcohol is chosen to fill into HiBi-PCF since it is an easy-filled liquid with a high temperature sensitivity. Here, an alcohol-filled HiBi-PCF is inserted into a FLM as a temperature sensing head. Birefringence change ΔB and length change ΔL of the alcohol-filled HiBi-PCF caused by temperature, leads a wavelength shifting of the resonant dips according to Eq. (3). The relationship between the dip wavelength change $\Delta\lambda_{dip}$, ΔB and ΔL is simply expressed as Eq. (5), $\Delta\lambda_{dip} = (\Delta BL + B\Delta L)/k$, where ΔB is the birefringence change caused by the thermo-optic effect, including that of the original HiBi-PCF and that of the filled alcohol, and ΔL is the length change caused by the thermo-expansion effect, which also includes the elongation of the original HiBi-PCF and the expansion of the filled alcohol. We neglect ΔB and ΔL caused by the HiBi-PCF itself because of a good thermal independence of the HiBi-PCF. Further, ΔL caused by the thermo-expansion of the filled alcohol is also ignored since the volume of alcohol filled into the air-holes of the HiBi-PCF is small. Thus, $\Delta\lambda_{dip}$ mainly depends on ΔB of the alcohol-filled HiBi-PCF. The birefringence-temperature dependence of the alcohol-filled HiBi-PCF is analyzed by using a full-vector finite element method (FEM). The diameters of the bigger and smaller holes are 7 and 3.2 μm, respectively, and the pitch length between centers of two adjacent holes is 5.46 μm, according to the HiBi-PCF used in experiment. The refractive index of pure silica and the filled alcohol is taken as 1.4457 and the empirical value which is calculated by an empirical equation according to [40]. Fig. 20 shows the empirical temperature dependence of the refractive index of alcohol and the theoretical temperature dependence of the birefringence of the alcohol-filled HiBi-PCF. With the temperature rising, the refractive index of alcohol decreases linearly, while the birefringence of the alcohol-filled HiBi-PCF increases linearly. The mode fields of the two orthogonal polarizations at 20 °C are shown in the insertion of Fig. 21. The birefringence of the alcohol-filled HiBi-PCF is calculated at 3.5×10^{-4} at 20 °C. P_t is defined as a thermo-optic constant on the birefringence of the alcohol-filled HiBi-PCF, which equals to the slope of the temperature dependence curve of birefringence and is calculated at 1.5×10^{-6} /°C. According to Eq. (2) and Eq. (5), the relationship between the resonant dip wavelengths shift $\Delta\lambda_{dip}$ and the temperature change ΔT can be deduced as

$$\Delta\lambda_{dip} = \Delta BL/k = \frac{LP_t}{k}\Delta T = \frac{\lambda_{dip}}{B}P_t\Delta T \tag{14}$$

Based on the above equation, the temperature sensitivity of the alcohol-filled HiBi-PCF FLM is related to λ_{dip}, P_t and B. A high temperature sensitivity depends on a long wavelength λ_{dip} of the measured resonant dip, a high thermo-optic constant P_t and a small birefringence B of the filled HiBi-PCF.

The HiBi-PCF used in the experiment is provided by Yangtze Optical Fibre and Cable Company. The HiBi-PCF has a birefringence of 10.2×10^{-4} at 1550 nm, and the length is 6.1 cm. After the HiBi-PCF filling with alcohol by air-holes capillary force, the birefringence of the PCF reduces significantly, which bring advantages on a larger wavelength space between two resonant dips and on a wider measurement range. Both ends of the alcohol-filled HiBi-PCF are spliced to conventional single-mode fiber (SMF) by using a regular arc splicing machine (Fujikura FSM 60).

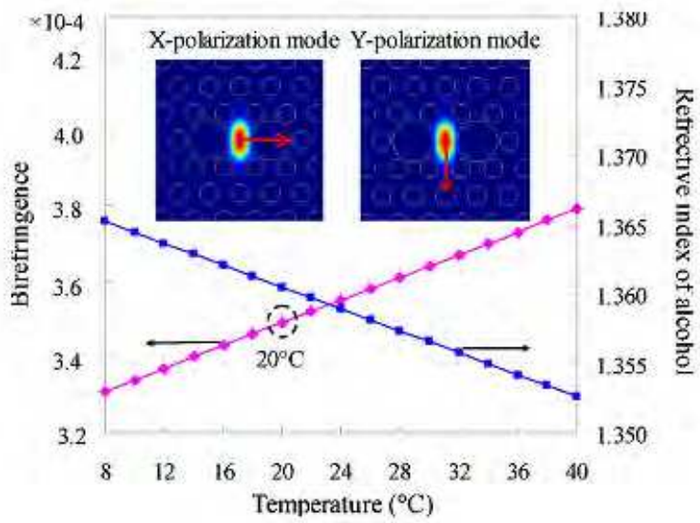

Fig. 20. Temperature dependence of the refractive index of alcohol and the birefringence of polarization mode fields of the alcohol-filled HiBi-PCF at 20 °C.

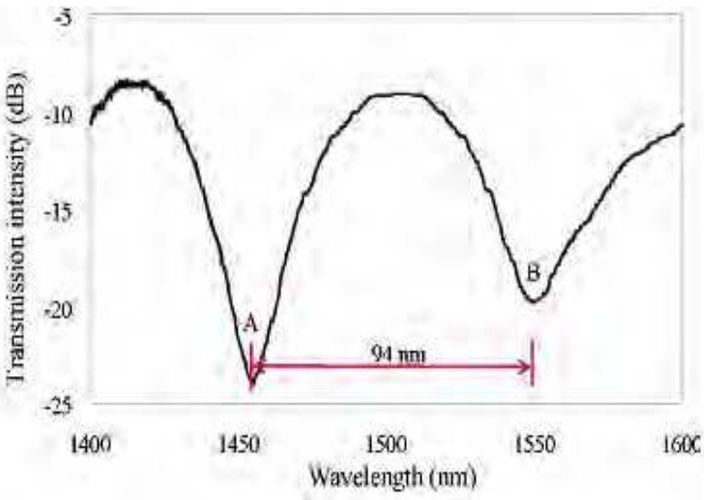

Fig. 21. Transmission spectrum of the alcohol-filled HiBi-PCF FLM at 20 °C.

Fig. 21 shows the transmission spectrum of the alcohol-filled HiBi-PCF FLM at room temperature (20 °C). Two resonant dips of the FLM display in the wavelength range from 1400 to 1600 nm. One is at the wavelength of 1455.8 nm (dip A) with 15.5 dB extinction ratio; the other is at about 1549.8 nm (dip B) with 10.5 dB extinction ratio. The wavelength spacing between these two dips is ~94 nm and the corresponding birefringence of the alcohol-filled HiBi-PCF is ~3.9×10^{-4} at 20 °C, which is close to the theoretical value (~3.5×10^{-4}). The little difference between the experimental and theoretical values may be caused by the error of air-holes geometry size of HiBi-PCF according the SEM.

In the experiment, the temperature characteristic of the alcohol-filled HiBi-PCF FLM is tested by placing the alcohol-filled HiBi-PCF of the FLM at a temperature-controlled container. Fig. 22 (a) and (b) show the transmission spectra of the alcohol-filled HiBi-PCF FLM at temperature range of 20 to 34 °C and 8 to 20 °C, respectively. Dip A red-shifts from 1455.8 to 1543.7 nm with temperature increasing gradually from 20 to 34 °C, at the same time, the extinction ratio of dip A decreases. While, dip B blue-shifts from 1549.8 to 1470.4 nm with the temperature decreasing gradually from 20 to 8 °C.

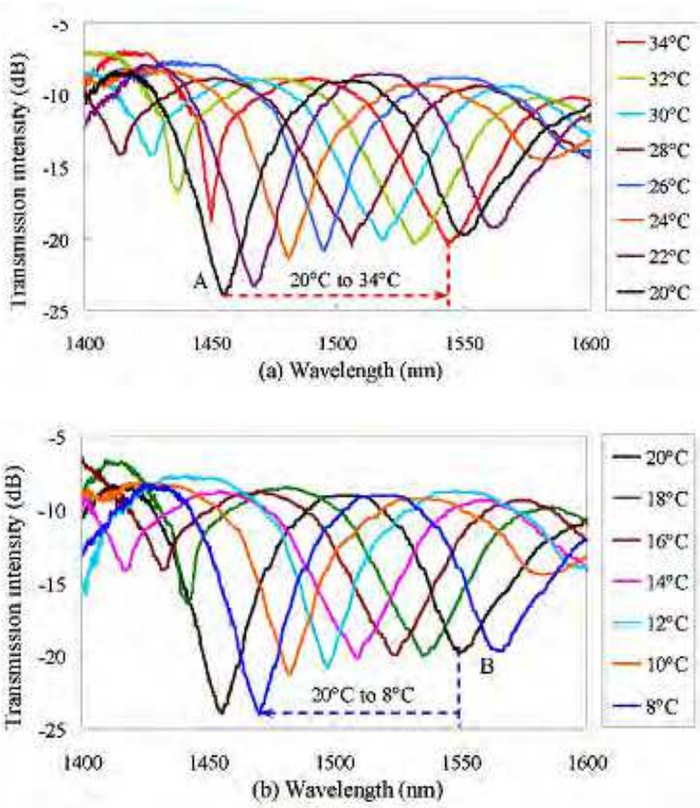

Fig. 22. Transmission spectra of the alcohol-filled HiBi-PCF FLM (a) when temperature increases from 20 and 34 °C and (b) when temperature decreases from 20 and 8°C.

Fig. 23 shows the experimental relationship between temperature and the resonant wavelength of dip A and dip B. The fitting curves can be expressed as y = 6.2176x+1331.7 for dip A and y = 6.6335x+1416.7 for dip B, and the high fitting degrees 0.9997 and 0.9995 mean the linearity of the resonant wavelength to temperature is excellent. The experimental

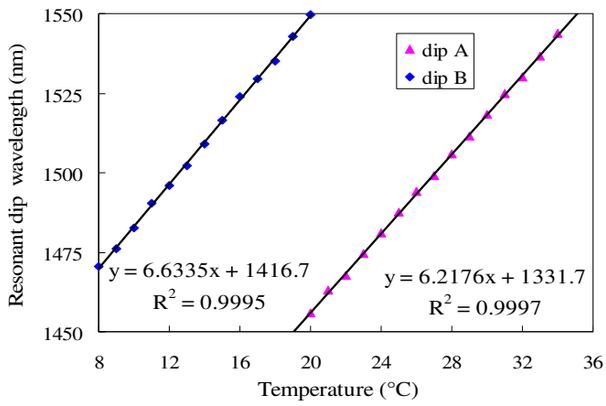

Fig. 23. The relationship between temperature and the resonant wavelength of dip A and dip B.

temperature sensitivities of dip A and dip B are ~6.2 nm/°C and ~6.6 nm/°C, respectively. And the theoretical sensitivities are ~6.1 nm/°C and ~6.5 nm/°C from Eq. (14). It is clear that the theoretical and the experimental results are in accordance. The temperature sensitivity of the alcohol-filled HiBi-PCF FLM is very high, and reach up to about 660 and 7 times higher than that of a FBG (~0.01 nm/°C) and that of the FLM made of a conventional HiBi fiber with a 72 cm length (~0.94 nm/°C) [10].

In practical uses, for a wider measurement range of temperature, the length L of the HiBi-PCF can be shortened in order to widen the spacing between two resonant dips based on $S = \lambda^2/BL$. For example, when the alcohol-filled HiBi-PCF is 1 cm, the spacing of the proposed FLM sensor is ~564 nm. It can be provided the measurement range of ~84 °C with the same temperature sensitivity ~6.6 nm /°C according to Eq. (14), in which the length of the sensing fiber is the same as the length of FBG sensing head and is shortened 72 times than that of the conventional HiBi-FLM temperature sensor.

5. Demodulation of sensors based on HiBi-PCF FLM [34]

All HiBi-PCF FLM sensors demonstrated above are based on monitoring the resonant wavelength variation of the FLM. In these configurations, a broadband light source and an optical spectrum analyzer (OSA) are needed, which cause the sensors expensive. In this part, we introduce a simple demodulation technology for a strain sensor based on HiBi-PCF FLM, which can also be used in other FLM based sensors. By utilizing the fact that the transmission intensity of a FLM at a fixed wavelength is strongly affected by the strain applied on a piece of HiBi-PCF in the FLM since the transmission spectrum of the FLM shifts with the applied strain, but the resonant dip (both wavelength and intensity) is insensitive to temperature, a low-cost temperature-insensitive strain sensor based on a HiBi-PCF FLM is achieved. The sensor uses a distributed-feedback (DFB) laser as the light source. Since the output intensity of the FLM is directly proportional to the applied strain, only an optical power meter is sufficient to detect strain variation, avoiding the need for an expensive OSA.

Since the HiBi-PCF is insensitive to temperature, the strain applied on the HiBi-PCF is an only influence factor on the transmission spectrum of the FLM. When an axial strain is applied on the HiBi-PCF, the phase difference of the FLM is changed, which is induced by

an elongation of the HiBi-PCF and the variation of birefringence of the HiBi-PCF caused by photoelastic effect. The relationship between the FLM phase change $\Delta\theta$ and the axial strain applied on the HiBi-PCF can be expressed as

$$\Delta\theta = \frac{2\pi}{\lambda}(LB + LP_e)\varepsilon \tag{15}$$

where $P_e = P_e^x n_x - P_e^y n_y$, and p_e^x and p_e^y are the effective photoelastic constant for the slow and fast axes, respectively.
So, when an axial strain is applied on the HiBi-PCF, the transmission spectrum of the FLM can be described as

$$T' = [1 - \cos(\theta + \Delta\theta)] / 2 \tag{16}$$

Fig. 24 shows the theoretical transmission spectra of the FLM at a free state and at the state of an axial strain (6000με) applied on the HiBi-PCF, which is gotten based on the equation (16). In theoretical calculation, the length and the birefringence of the HiBi-PCF are taken as L = 79.5 mm and B = 8.5×10^{-4}, respectively, in accordance to the experimental data. P_e of the HiBi-PCF is assumed to $P_e = -2.24\times10^{-4}$ [16], which best fits the experiment. As shown in Fig. 25, the transmission spectrum of the FLM shifts to longer wavelength since the phase matching condition is changed when an axial strain is applied on the HiBi-PCF. Therefore, the applied strain can be gotten by monitoring the resonant wavelength shift of the FLM through using a broadband light source and an OSA in a high cost. The theoretical sensitivity of strain based on monitoring the resonant wavelength shift is obtained at 1.1 pm/με.

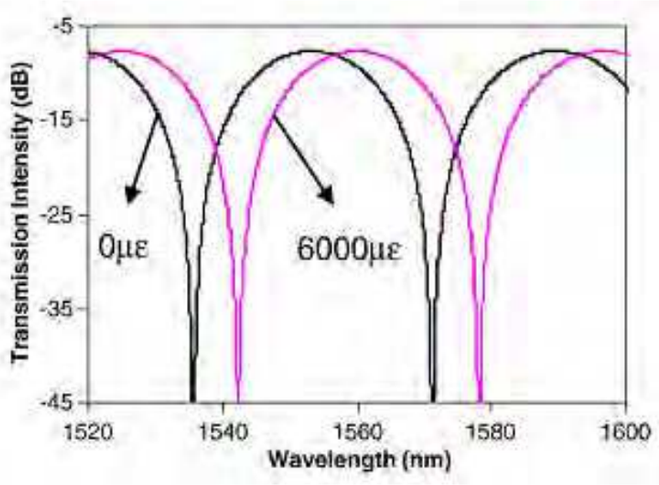

Fig. 24. Theoretical transmission spectra of the FLM at a free state and at the state of an axial strain (6000 με) applied on the HiBi-PCF.

Meanwhile, the transmission intensity at a fixed wavelength changes when the transmission spectrum of the FLM shifts with the strain applied on the HiBi-PCF. Thus, the information of the applied strain can be also gotten by monitoring the transmission intensity. The HiBi-PCF FLM sensor based on intensity measurement can be achieved in a low cost by using a DFB laser and an optical power meter, instead of an expansive broadband source and an

OSA. When an axial strain is applied on the HiBi-PCF, the FLM transmission intensity at a fixed wavelength can be described as

$$T_0^{'} = [1 - \cos(\theta_0 + C_0\varepsilon)] / 2 \tag{17}$$

where $\theta_0 = \frac{2\pi}{\lambda_0} LB$, $C_0 = \frac{2\pi}{\lambda_0}(LB + LP_e)$. It is clear that, the transmission intensity of the FLM at a fixed wavelength varies accordingly with the applied strain. The transmission intensity variation of the FLM with the change of the axial strain applied on the HiBi-PCF can be deduced as

$$\frac{dT_0^{'}}{d\varepsilon} = \frac{1}{2} C_0 \sin(\theta_0 + C_0\varepsilon) \tag{18}$$

Fig. 25 is the theoretical relationship between the transmission intensity of the FLM sensor and the applied axial strain at three different wavelengths, which are gotten from the equation (17). As shown in the Fig. 24, the transmission intensity of the FLM at a fixed wavelength is approximately a periodic function of the axial strain applied on the HiBi-PCF. The strain spacing is about 33000 με. This means the maximal measurement range is about 16500 με, in which the relationship between the applied strain and the transmission intensity of the FLM is a proportional dependence. When the strain is measured from 0 με, the measurement range of the applied strain is different for the different fixed wavelength. When the fixed wavelength is chosen at the resonant wavelength (1535.6 nm), the measurement range of the strain is maximum, which is from 0 to 16500 με.

Fig. 26 is the enlarged drawing of the circle part in Fig. 25. Fig. 26 shows that all of the transmission intensity of the FLM at four different wavelengths (1530 nm, 1532 nm, 1545 nm and 1547 nm) are proportional to the applied strain, when the strain is in the range of 0 ~ 6000 με. The strain sensitivity is in positive when the fixed wavelength (1530 nm and 1530 nm) is shorter than the resonant wavelength (1535.6 nm) of the FLM; on the other hand, the strain sensitivity is in negative when the fixed wavelength (1545 nm and 1547 nm) is longer than the resonant wavelength (1535.6 nm) of the FLM.

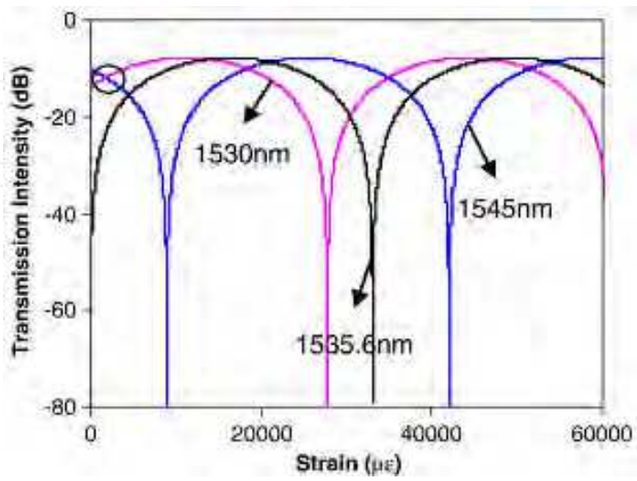

Fig. 25. Theoretical strain dependence of the transmission intensity of the FLM at different wavelengths.

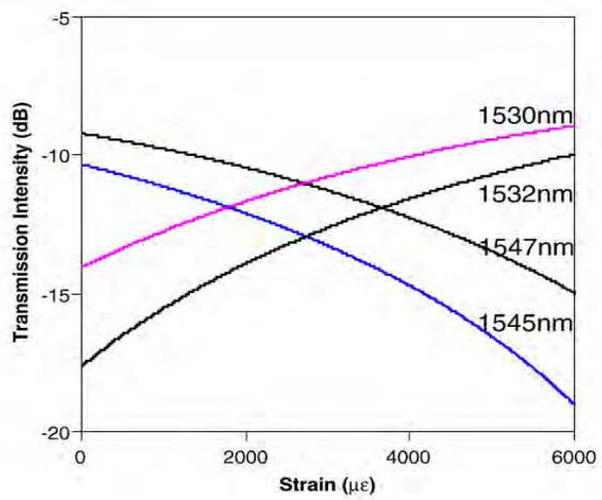

Fig. 26. Theoretical strain dependence of the transmission intensity of the FLM at different wavelengths in the strain range of 0~6000 με.

Fig. 27 shows the transmission spectrum of the HiBi-PCF FLM. The HiBi-PCF has a birefringence B of ~8.5×10^{-4} at 1550 nm, and the length L of 79.5 mm. The corresponding wavelength spacing between transmission peaks (or transmission dips) is about 35.6 nm, and the extinction ratio is nearly 26 dB. Fig. 28 shows the strain characteristics of the FLM at different strain. The whole transmission spectrum shifts toward longer wavelength with the applied strain increasing because the length of the HiBi-PCF increases with the axial stretching and the birefringence of the HiBi-PCF decreases due to the photoelastic effect of the fiber. When the strain sensor is based on the resonant wavelength monitoring, the strain sensitivity with wavelength which is the slope of the curve, is estimated to be 1.1 pm/με as shown in Fig. 39. Experimental results are identical with the theoretical analysis. When an OSA with a wavelength resolution of 10 pm is used, the strain resolution is about 9.1 με.

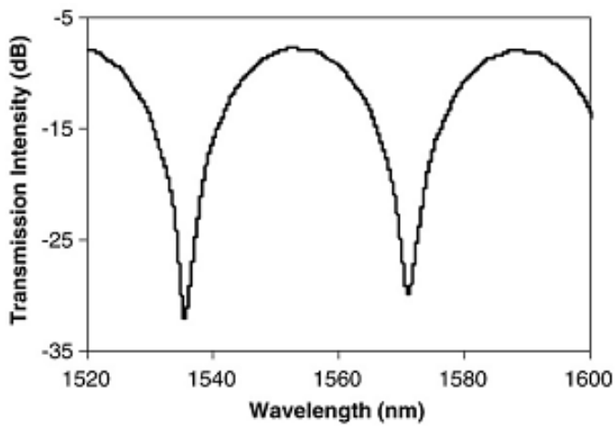

Fig. 27. Experimental transmission spectrum of the HiBi-PCF FLM.

When the strain sensor is based on the transmission intensity measurement, a single wavelength source such as a wavelength tunable laser or a DFB laser is used as a light source. The HiBi-PCF FLM sensor based on optical intensity measurement is measured with

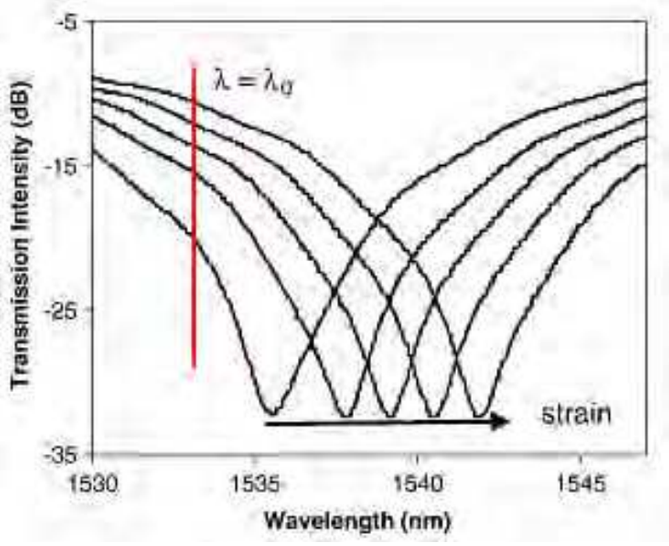

Fig. 28. Experimental transmission spectra of the FLM at different strain applied on the HiBi-PCF (from left to right, the strain: 0, 2137, 3357, 4565 and 5770 με, respectively).

a tunable laser source (Agilent 81689 A) and a power meter (Agilent 81634 A). The wavelength of the tunable laser is near the resonant wavelength of the FLM and hence the output light intensity from the FLM is directly related to the FLM's transmission at the wavelength of the DFB laser. Since the FLM's transmission is insensitive to temperature, the output power is only affected by the transmission spectrum change caused by the strain applied on the HiBi-PCF. Fig. 30 shows the measured and theoretical relationship between the output intensity of the FLM sensor and the applied axial strain for various laser wavelengths. It's clear that the strain sensitivity with intensity is related to the wavelength of the used laser source. In our experiment, a tunable laser is used for easiness of wavelength adjustment. In practice, a DFB laser with appropriate wavelength would be better for the purpose of reducing cost.

As shown in Fig. 30, for laser wavelengths of 1530 nm and 1532 nm, which are shorter than the resonant wavelength (1535.6 nm) of the FLM, the output intensity increases with applied strain and the strain sensitivity is positive. Meanwhile, for laser wavelength longer than the resonant wavelength (1535.6 nm), the output intensity decreases with the applied strain and the intensity sensitivities are negative. Fig. 30 also shows the theoretical curves of the relation between the output intensity and the applied strain. The experimental results are in a good agreement with the theoretical analysis.

From the equation (17), the output intensity in response of the strain can be expressed in $T = [1-\cos(\theta_0+C_0\varepsilon)]/2$. When laser wavelengths are 1530 nm and 1545 nm, the theoretical relationships between the output intensity and the applied strain are $T_{1530} = [1-\cos(277+203\varepsilon)]/2$ and $T_{1545} = [1-\cos(274+201\varepsilon)]/2$, respectively. The coefficients θ_0 and C_0 of the above equations are different since the wavelength is different. In the above theoretical equations, dispersion effect on the B is ignored. The experimental and theoretical results are identical, and the fitting degrees between them are obtained highly as $R^2 = 0.997$ at the wavelength 1530 nm and $R^2 = 0.994$ at the wavelength 1545 nm, respectively. Furthermore, the strain sensitivity is various with the applied strain. When the applied strain is 3000 με, the strain sensitivity is 2.7 dB/1000με at 1530 nm and -3.2dB/1000με at 1545 nm. When an

optical power meter with an intensity resolution of 0.01 dB is used, a strain resolution of 3.7 με at 1530 nm and 3.1 με at 1545 nm is achieved, which is about 2.5 times higher than that of the strain sensor based on the resonant wavelength measurement.

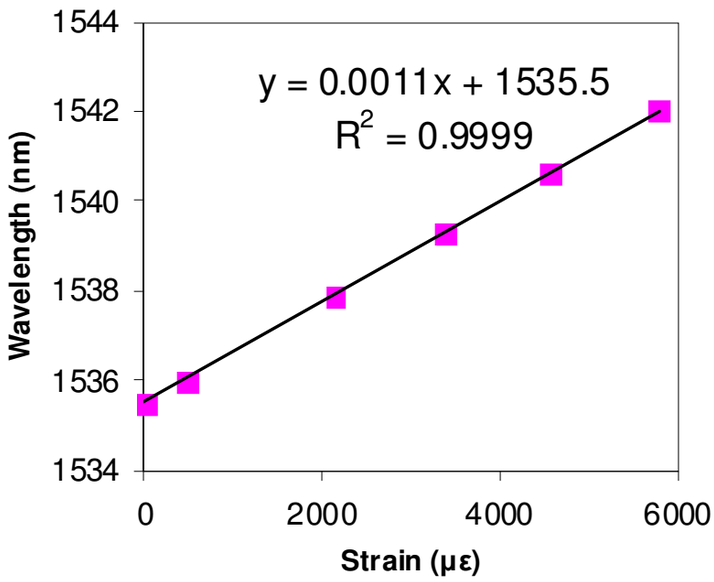

Fig. 29. The experimental relationship between the of the FLM at different wavelengths. Lines: theoretical curves. Pointes: experimental data.

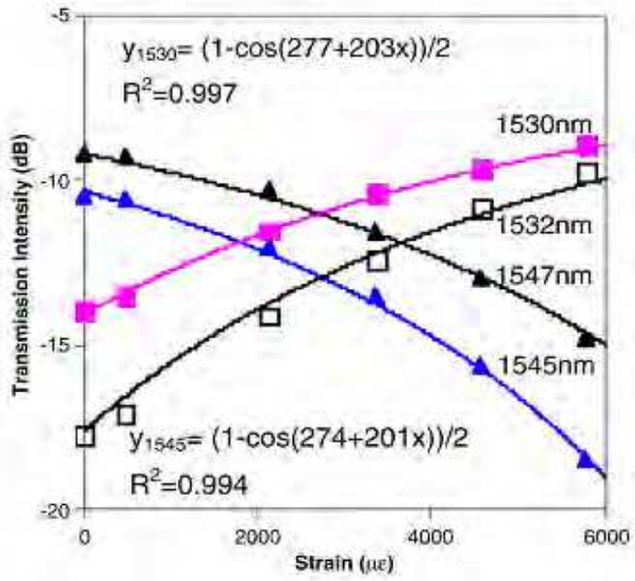

Fig. 30. Strain dependence of the transmission intensity wavelength of the transmission peak near 1535.6 nm of the FLM and the strain applied on the HiBi-PCF.

6. Multiplexing of HiBi-PCF based Sagnac interferometric sensors [35]

In this part, three multiplexing schemes for PM-PCF based Sagnac interferometric sensors are presented. The first scheme is to multiplex sensors in the wavelength domain using coarse wavelength division multiplexers (CWDMs). The sensing signal from each sensor can be measured within a specific wavelength channel of the CWDM. The second scheme is to multiplex sensors by connecting them in series along a single fiber. It is simple in terms of system architecture as no additional fiber-optic components are needed. The third scheme is to multiplex sensors in parallel by using fiber-optic couplers. The sensing information of the first multiplexing technique can be obtained by direct measurement such as with an optical spectrum analyzer. For the serial and parallel multiplexing, signal processing methods are required to demultiplex the complex sensing signal. Two mathematical transformations, namely the discrete wavelet transform (DWT) and the Fourier transform (FT), are used independently to convert the multiplexed sensing signal back to their constituent sensor signals. These two transform methods are experimentally demonstrated via two multiplexed Sagnac interferometric sensors. Their operating principles, experimental setup, and overall performance are discussed. In the part of 4.2, we have demonstrated the utilization of PM-PCF based Sagnac interferometers for pressure sensing [29]. Similar pressure sensing experiments were performed here for the purposes of demonstration and verification of the multiplexing schemes as well as the demultiplexing methods.

6.1 Multiplexing technique base on CWDM

Wavelength division multiplexing is a direct multiplexing technique that can be readily implemented into Sagnac interferometric sensors. Since the output interference spectra of all the sensors cover the whole bandwidth of the light source, individual sensor signals can be physically separated by CWDMs into different wavelength channels. The experimental setup of two multiplexed sensors using CWDMs is illustrated in Fig.31. It includes a

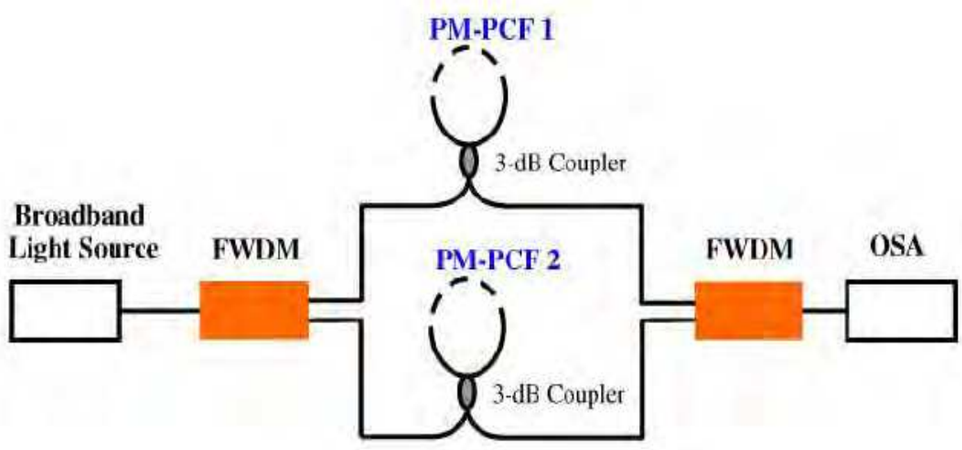

Fig. 31. Experimental setup of FWDM multiplexing technique for two PM-PCF based Sagnac interferometric sensors.

broadband light source, an OSA, two identical filter wavelength division multiplexers (FWDMs) with the two output ports having respective operation range in the C and L bands (1500~1562 nm/1570~1640 nm). The two Sagnac interferometric sensors, PM-PCF1 and PM-PCF2, have effective PM-PCF lengths of 40 cm and 80 cm, respectively. After the broadband light was launched into the first FWDM, the light was split into C and L bands. These two bands of light then illuminated the two sensors separately and were recombined by the second FWDM.

Figure 32 shows the output spectrum of the two Sagnac interferometric sensors multiplexed by FWDM. From the figure, sensors PM-PCF 1 and PM-PCF 2 are found in the L band and C band, respectively. The FWDMs are shown to have good flatness in their operating wavelength range. There is an abrupt discontinuity at the edges of the two FWDMs at around 1562 nm–1570 nm, where such range should be excluded from measurements. By measuring the shifts of individual transmission minima (or maxima) of the two Sagnac interferometric sensors within their corresponding wavelength ranges, sensing information of both sensors can be obtained.

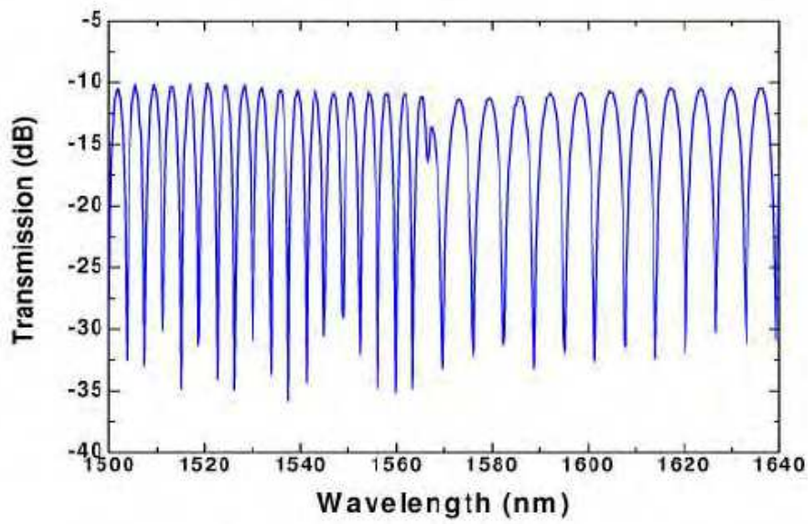

Fig. 32. Output Spectrum of the CWDM multiplexing technique for PM-PCF based Sagnac interferometric sensor.

6.2 Multiplexed in series along a single fiber with transmitted signals

The second multiplexing scheme is to multiplex Sagnac interferometric sensors in series along a single fiber. Similar concatenated sensor configuration has been employed previously in optical filtering [41], and in strain and temperature discrimination [42]. However, in both cases, multiplexing was not the main focus, and so the techniques of multiplexing were not studied. Figure 33 illustrates such a scheme by simply cascading the sensors together. For K Sagnac interferometric sensors multiplexed in series, the output spectrum is given by,

$$\frac{P_{output}}{P_{input}} = 10Log\prod_{k=1}^{k}\{\frac{1}{2}L_k[1-\cos(\frac{2\pi}{S_k}\lambda+\theta_k)]\}[dB] \quad (19)$$

where L_k, S_k, θ_k are the loss, the period of the output spectrum and the initial phase of the k-th sensor, respectively. Note that the output spectrum is the multiplication of all individual sensor signals.

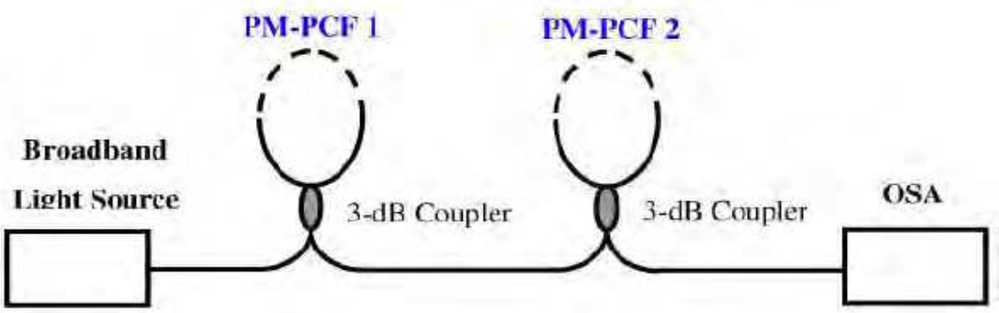

Fig. 33. Experimental setup of in series multiplexing technique for PM-PCF based Sagnac interferometric sensor.

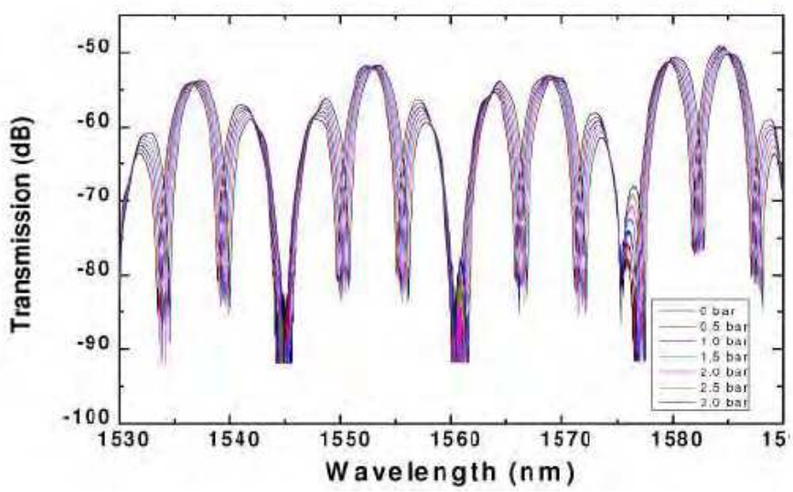

Fig. 34. Output transmission spectra of the two multiplexed Sagnac interferometric sensors in series with one sensor under applied pressure variations.

In the experimental demonstration, two sensors were spliced together adjacent to each other in series. The effective lengths of PM-PCF1 and PM-PCF2 were 20 cm and 60 cm, respectively. PM-PCF1 was placed freely on a table, while PM-PCF2 was placed inside a sealed pressure chamber. Pressure was applied to PM-PCF2 from 0–3 bars in steps of 0.5 bar, and was measured by a pressure gauge (COMARK C9557). Figure 34 shows the output spectra of various pressure values measured by the OSA. In principle, to obtain the sensing

information, the wavelength shift of the transmission minima of each sensor needs to be determined. However, as can be seen, the multiplexed sensor signal is more complex, and so simply tracing the initial phase may not yield accurate results. Thus, in order to separate the multiplexed signals, the DWT and FT methods were used independently to demultiplex the sensing signals. They worked by transforming the signals into another domain, such that each individual sensor signal can be easily identified, and their phase shifts measured.

6.3 DWT demultiplexing method

The principle of the DWT demultiplexing method has been outlined in Ref. [43].When DWT is applied to a signal, it is decomposed and halved into high and low frequency components, represented as detail and approximation coefficients, respectively. This is similar to applying both a high-pass and a low-pass filter simultaneously to a signal. Then, the approximation coefficients (i.e., low frequency components) of the signal can be further decomposed into 2nd-level detail and approximation coefficients. This iterative process continues until all individual sensor signals are separated and appear on different wavelet levels. In other words, it continues until the spatial frequency of the sensing signals matches with the frequency range at which the wavelet level represents. Figure 35 shows the extracted detail coefficients of the two sensors at different wavelet levels. By tracking their phase shifts, the response of the two sensors under various pressure levels can be detected. Figure 36(a) shows the phase shifts of the two sensors as a function of applied pressure. It is clear that PM-PCF2 shifted linearly with applied pressure, while PM-PCF1 remained about the zero shift position. The crosstalk between the two multiplexed sensor signals was also measured. The crosstalk given here is the ratio of the phase shift of PM-PCF1 (no pressure applied) to that of PM-PCF2 (pressured applied), and is shown in Fig. 36(b). It should be noted that, the crosstalk measurement represented here includes other sources of errors, such as measurement error and ambient noise. As can be seen from the figure, the crosstalk between the two sensors is less than 5% and decreases progressively at higher pressure values. This means the absolute crosstalk values are quite stable for the measured pressure range, and implies that the errors are mainly due to sources other than the actual crosstalk between the two sensors. On the other hand, if the crosstalk measurement shows a trend that correlates with the applied pressure, this would mean there is actual crosstalk present in the multiplexed sensor system.

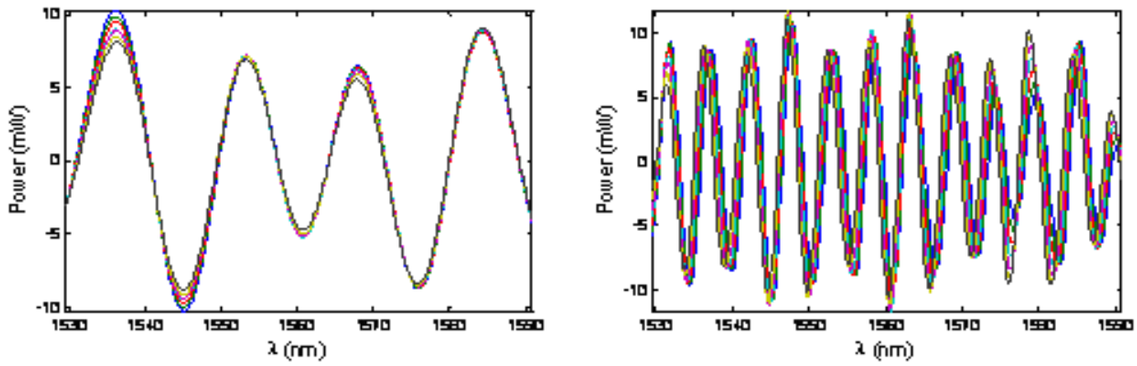

Fig. 35. Sensing signals of the two Sagnac interferometric sensors extracted using the wavelet method.

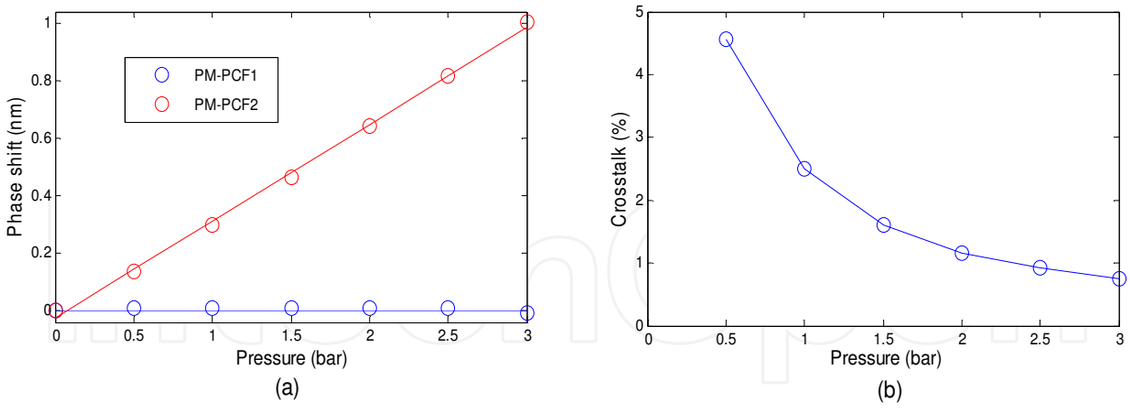

Fig. 36. (a) The wavelength shift as a function of pressure variation for the two Sagnac interferometric sensors,(b) sensing signal crosstalk of the two Sagnac interferometric sensors.

6.4 FT demultiplexing method

Besides the DWT, we also employed the FT method and the operating principle can be found in Ref. [44].The FT method works by transforming the multiplexed sensing signal from the original (wavelength) domain, into its dual (spatial frequency) domain, and is represented in the FT magnitude and phase spectra. Since the multiplexed signal is periodic, each individual sensor appeared as an finite amplitude peak in the FT magnitude spectrum; residing at a position dependent on the spatial frequency of the original sinusoidal signals. Thus, provided no two sensors have the same spatial frequency, each sensor can be distinctly identified. Normally, there are two ways of tracing the measurand-induced changes of individual sensors: (i) if the spatial-frequencies of the sensors change, measurands can be detected by the amount the amplitude peaks shift in the magnitude spectrum; and (ii) if the phase of the sensors change (and not the spatial-frequencies), measurands can be detected by the change of slope of the phase spectrum over the region corresponding to the amplitude peaks of the sensors in the magnitude spectrum. For the PM-PCF Sagnac interferometric sensors, when pressure was applied, the phase of the signals shifted proportionally while the spatial frequencies have no noticeable change, and so the second method applies. Figure 37 gives the FT magnitude and phase spectra of the multiplexed sensing signals after taking the FT. The corresponding regions of phase for the two sensors are shown in Fig.38. From the figure, one can see that PM-PCF1 is held constant (no noticeable change in the phase slope), while PM-PCF2 is under a varying amount of applied pressure which resulted in a gradual change of the phase slope. The calculated equivalent wavelength shift and crosstalk between the two sensors are shown in Figs. 39(a) and 39(b), respectively. From the figure, the maximum crosstalk is~5%, which is considered small.

6.5 Multiplexed in parallel by using coupler with reflected signals

The third multiplexing scheme is to multiplex Sagnac interferometric sensors in parallel, and is illustrated in Fig.40.The effective lengths of PM-PCF1 and PM-PCF2 are 20 cm and 60 cm, respectively. The source light is split equally by the 3-dB coupler into two paths to illuminate the two sensors separately. The sensing signals reflected back from the two

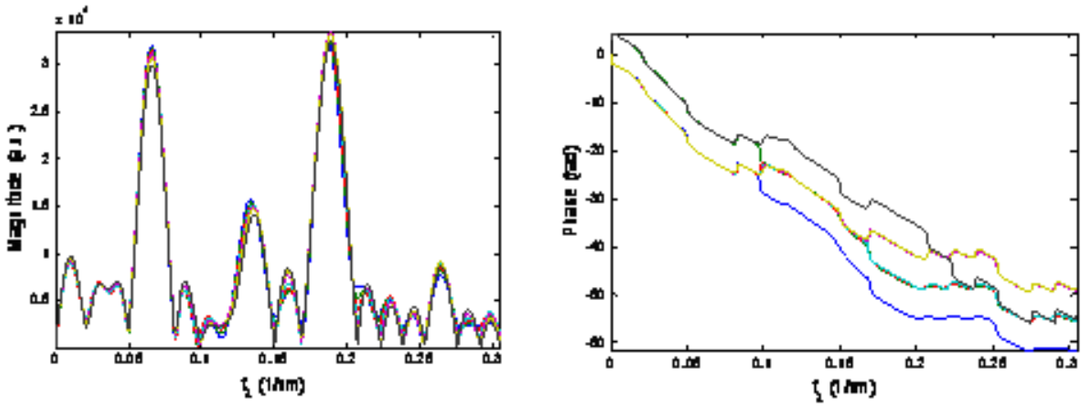

Fig. 37. Magnitude spectra and phase spectra of the sensing signal under Fourier transformation.

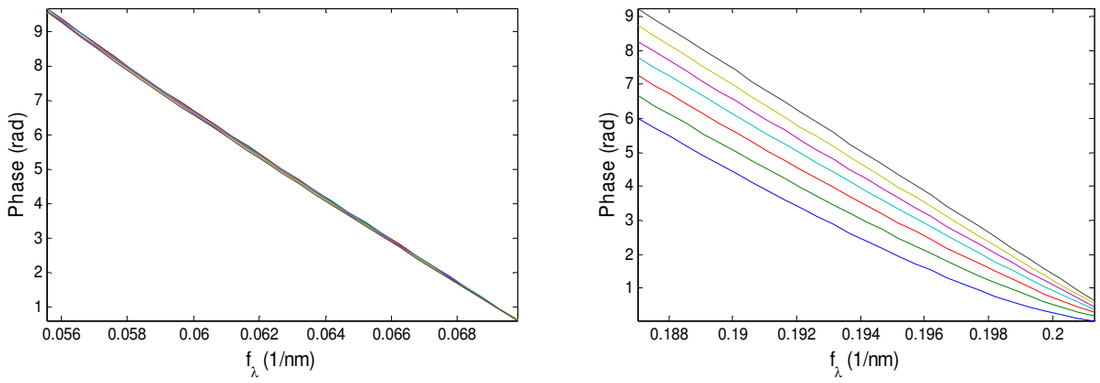

Fig. 38. Phase shift of the sensing signal from the two Sagnac interferometric sensors.

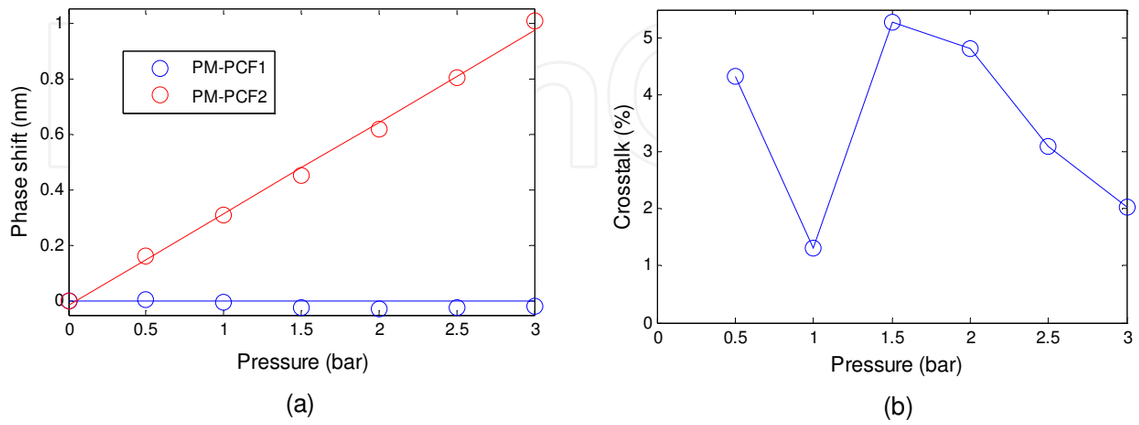

Fig. 39. (a) The wavelength shifts as a function of pressure variation for the two Sagnac interferometric sensors, (b) sensing signal crosstalk of the two Sagnac interferometric sensors.

sensors are then coupled together by the same 3-dB coupler, and were measured with an OSA. The unused ends of the sensors were coiled in small loops to minimize Fresnel reflections. As compared to the serial multiplexing scheme, it required an additional 3-dB coupler. Note that the reflected sensing signals were taken instead of the transmitted signals, and there were two reasons for it. First, it helped to use one less 3-dB coupler to combine individual sensor signals at the output side and so reduced the system cost and complexity. Second, the reflected signal spectrum is, mathematically, the complement of the transmitted spectrum; and since the spectrum is of the form of sinusoidal pattern, the only difference is the phase angle of π. For K Sagnac interferometric sensors multiplexed in parallel, the output spectrum is given by,

$$\frac{P_{output}}{P_{input}} = 10Log_{10}\sum_{k=1}^{k}\{\frac{1}{2}L_k R_k[1+\cos(\frac{2\pi}{S_k}+\theta_k)]\}[dB] \quad (20)$$

where R_k, L_k, S_k, θ_k are the coupling ratio, the loss, the period of the output spectrum and the initial phase of the k-th sensor, respectively. Note that the output spectrum is the arithmetic sum of all individual sensor signals, as opposed to multiplication in the serial multiplexing case.

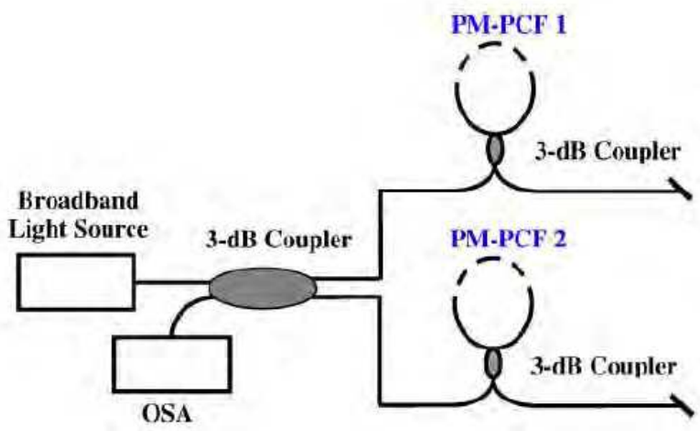

Fig. 40. Experimental setup of in parallel multiplexing technique for PM-PCF based Sagnac interferometric sensors.

As an experimental demonstration, a similar pressure sensing experiment to the previous multiplexing scheme was performed. Figure 41 shows the output spectra, with PM-PCF1 placed freely on the table and PM-PCF2 placed inside the pressure chamber. Again, we employed both the DWT and FT methods independently to demultiplex the sensing signal.

6.6 DWT demultiplexing method

After taking the DWT of the multiplexed sensing signal, Fig.42 shows the detail coefficients of the two sensors at different wavelet levels. It is apparent from the figure that PM-PCF 1 remained almost constant, while PM-PCF2 can visibly be seen to have had the whole signal shifted. The phase shifts of the two sensors and the corresponding crosstalk measurement are shown in Figs. 43(a) and 43(b), respectively. The crosstalk between the two sensing signals is indeed very small, with a maximum value of less than 2%.

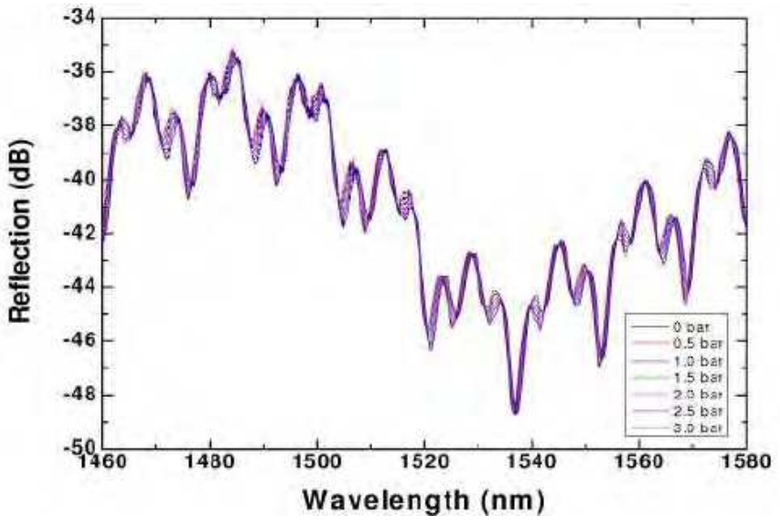

Fig. 41. Output transmission spectra of the two multiplexed Sagnac interferometric sensors in parallel with one sensor under applied pressure variations.

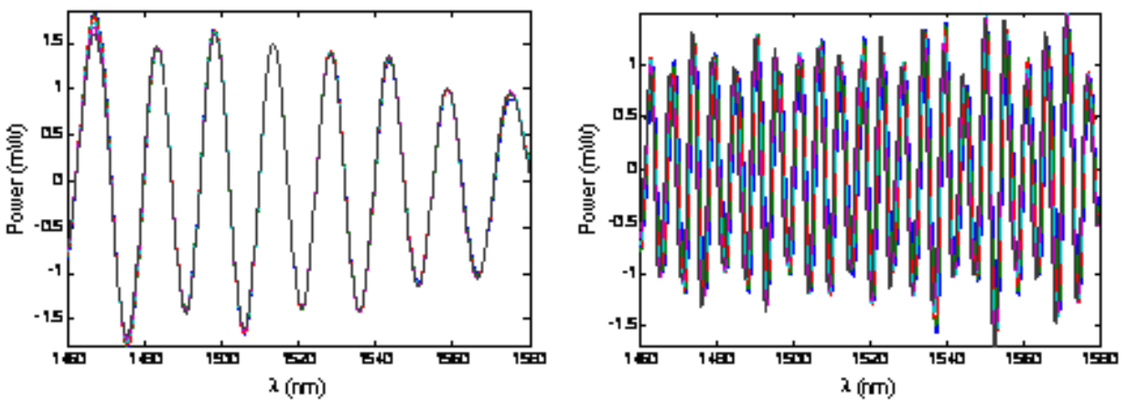

Fig. 42. Sensing signals of the two Sagnac interferometric sensors extracted using the wavelet method.

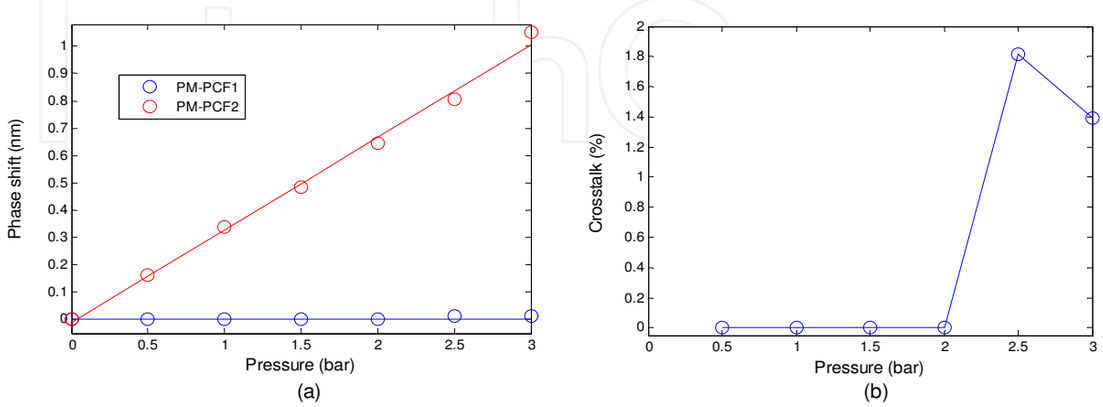

Fig. 43. (a) The wavelength shifts as a function of pressure variation for the two Sagnac interferometric sensors, (b) sensing signal crosstalk of the two Sagnac interferometric sensors.

6.7 FT demultiplexing method

With the FT method applied, Fig. 44 gives the FT magnitude and phase spectra of the multiplexed sensing signals. The corresponding regions of phase for the two sensors are illustrated in Fig.45. From the figure, one can notice that PM-PCF1 has no noticeable change in the phase slope, while PM-PCF2 experienced pressure changes which resulted in a gradual change in the phase slope. The calculated equivalent wavelength shifts and the corresponding crosstalk measurement are shown in Figs. 46(a) and 46(b), respectively. Again, the crosstalk is very small, with a maximum of less than 3%.

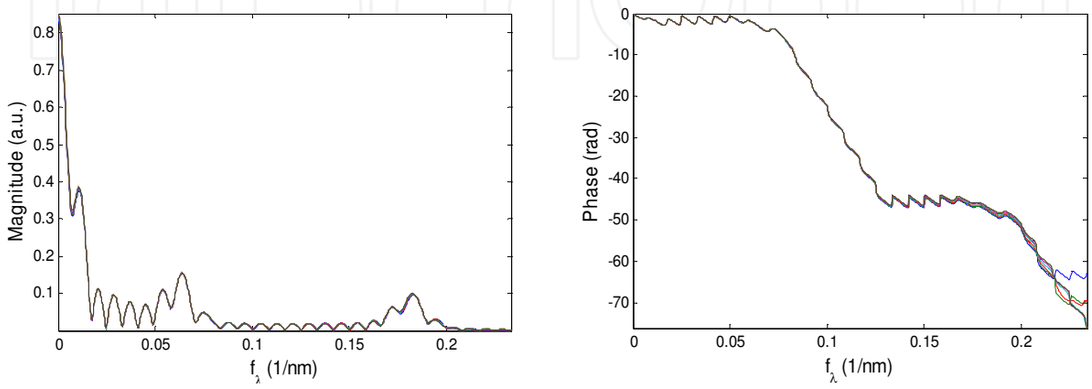

Fig. 44. Magnitude spectrum and phase spectrum of the sensing signal under Fourier transformation.

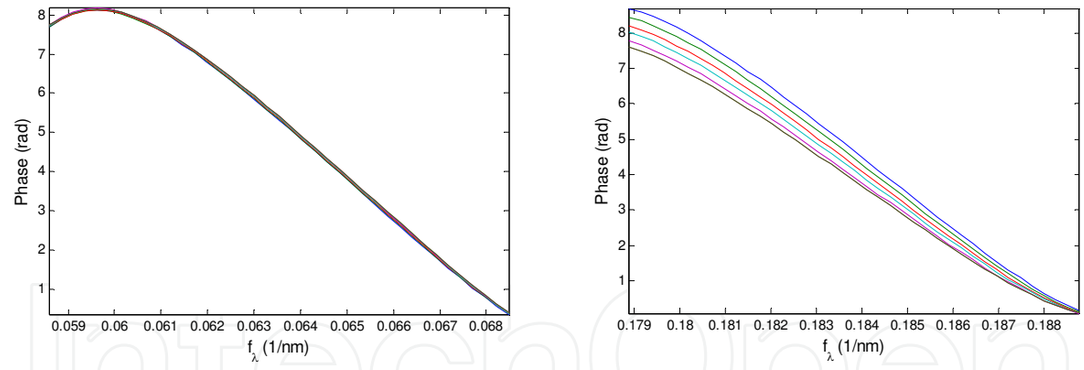

Fig. 45. Phase shift of the sensing signal from the two Sagnac interferometric sensors.

6.8 Discussions

Each of the three multiplexing schemes has its own characteristics and is suitable for different applications. The CWDM scheme enables easy real-time system implementation. It provides a direct measurement without the need for dealing with crosstalk between signals from different channels. The number of sensors that can be multiplexed is limited by the available channels of the CWDM at a fixed light source bandwidth. Although with more channels, more sensors can be multiplexed; the bandwidth of each channel becomes narrower. In principle, the minimum bandwidth of each channel has to be larger than the period of the sensor signal, plus a bit of guard band between channel edges to avoid erroneous results due to signal discontinuities.

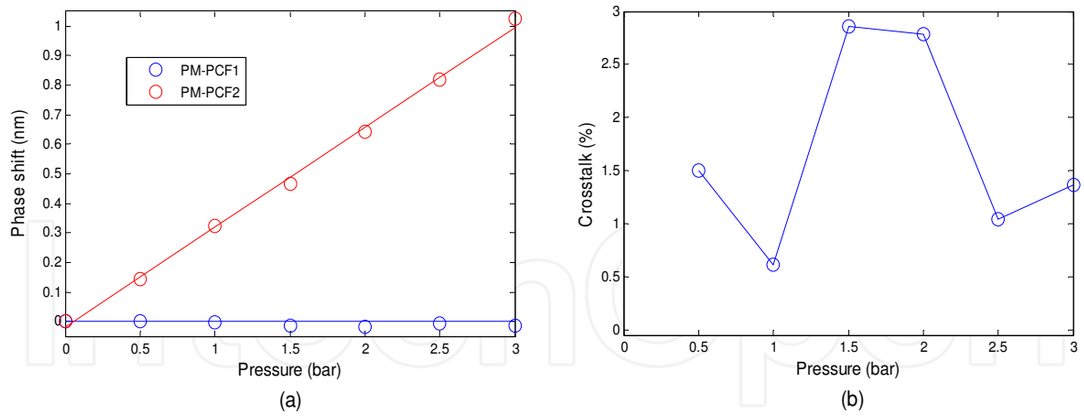

Fig. 46. (a) The wavelength shifts as a function of pressure variation for the two Sagnac interferometric sensors, (b) sensing signal crosstalk of the two Sagnac interferometric sensors.

For the serial multiplexing scheme, no additional fiber-optic components are needed. The sensors are multiplexed easily by connecting them together one by one, which makes this scheme the simplest in terms of sensor system architecture. The number of sensors that can be multiplexed is mainly limited by the splicing loss between PM-PCFs and SMFs. On the other hand, for the parallel multiplexing scheme, it requires the addition of fiber couplers, which makes the system architecture relatively more complex and increases the total system cost. In addition, it increases the insertion loss due to splicing and fiber couplers. Nevertheless, the errors and adverse effects are also less because individual sensor signals are added rather than multiplied, and so they do not suffer from spectral shadowing and nonlinear mapping as is found in the serial multiplexing scheme [42]. It is evident from our experiments that parallel multiplexing has less crosstalk (with other sources of errors included) than that of serial multiplexing. It should be pointed out that the measurement errors due to fluctuations in the applied pressure played a role in our results, which can be noticed in their deviation from ideal values. This implies the intrinsic crosstalk is believed to be quite low.

There is a consideration when using the DWT and FT methods to demultiplex the sensor signals obtained from the serial and parallel multiplexing schemes. The effective length of PM-PCFs must be properly chosen not to be too close to each other in order to avoid overlap after performing the transformations. However, it is not an issue for the CWDM scheme because signals from sensors are well distinguished by each channel. These three multiplexing schemes can be implemented together to further increase the number of sensors.

For example, within each channel in the CWDM, sensors can be multiplexed in series or in parallel. This combined configuration cannot only increase the number of sensors by several times, but also maximizes the full use of the light source bandwidth. To sum up, from practicability point of view, the CWDM scheme is among the easiest and simplest, whereas serial multiplexing is more practical in real applications. On the other hand, parallel multiplexing offers slightly better performance in terms of crosstalk and measurement errors. At present stage, the main limitations on the last two multiplexing schemes are the insertion loss. The presented multiplexing schemes, together with the two demultiplexing methods, are not only limited to use for PM-PCF Sagnac interferometric sensors. Indeed, they can be applied in any PCF sensor that has sinusoidal patterns. This will be one step closer towards a more practical sensing system using PCF based sensors.

7. Summary

In this chapter, we have introduced and demonstrated the basic operation principle of FLMs, and their applications in optical devices and in optical sensors, which include:

i. Temperature-insensitive interferometer based on HiBi-PCF FLM. The temperature-insensitivity of the FLM is improved 55 times by using the HiBi-PCF, mainly because the temperature coefficient of birefringence in PCF is measured to be 30 times lower than that of conventional PMF;
ii. Temperature-insensitive strain sensor based on HiBi-PCF FLM. Strain measurement with a sensitivity of 0.23 pm/με is achieved, and the measurement range, by stretching the PM-PCF only, is up to 32 mε. The strain measurement is inherently temperature insensitive due to the great thermal stability of PM-PCF based Sagnac interferometers. That improves the accuracy of strain measurement and eliminates the requirement for temperature compensation;
iii. Pressure sensor realized with HiBi-PCF based Sagnac interferometer. The Sagnac loop itself acts as a sensitive pressure sensing element, making it an ideal candidate for pressure sensor. Pressure measurement results show a sensing sensitivity of 3.42 nm/MPa, which is achieved by using a 58.4 cm PM-PCF-based Sagnac interferometer. Important features of the pressure sensor are the low thermal coefficient and the exceptionally low bending loss of the PM-PCF, which permits the fiber to be coiled into a 5mm diameter circle. This allows the realization of a very small pressure sensor;
iv. Compact and highly sensitive temperature sensor based on an alcohol-filled HiBi-PCF FLM. Due to the high temperature sensitivity of the filled alcohol, an alcohol-filled HiBi-PCF FLM with an extremely high sensitivity on temperature are presented Experimental results show that the sensitivity is as high as 6.6 nm/°C, which is 660 and 7 times higher than that of a FBG and that of the FLM made of a conventional HiBi fiber;
v. Demodulation of sensors based on HiBi-PCF FLM. The sensor demodulation is based on the intensity measurement, in which a distributed-feedback (DFB) laser is used as the light source. Since the output intensity of the FLM is directly proportional to the applied strain, only an optical power meter is sufficient to detect strain variation, avoiding the need for an expensive OSA;
vi. Multiplexing of HiBi-PCF based Sagnac interferometric sensors. Three multiplexing schemes are presented for HiBi-PCF based Sagnac interferometric sensors. The first technique is wavelength division multiplexing using coarse wavelength division multiplexers (CWDMs) to distinguish signals from each multiplexed sensor in different wavelength channels. The other two schemes are to multiplex sensors in series along a single fiber link and in parallel by using fiber-optic couplers. While for the CWDM scheme, the multiplexed sensing signal can be obtained by direct measurement; for the other two multiplexing techniques, the sensing signal is more complex and cannot be easily demultiplexed. Thus, some signal processing methods are required. In this regard, two mathematical transformations, namely the discrete wavelet transform and Fourier transform, have been independently and successfully implemented into these two schemes. The operating principles, experimental setup, and overall performance are discussed.

8. References

[1] V. Vali and R. W. Shorthill, "Fiber ring interferometer," Appl. Opt. vol.15, pp.1099–1103 (1976).

[2] D. B. Mortimore, "Fiber loop reflectors", J. Lightwave Technol., vol. 6, pp. 1217-1224, (1988).

[3] X. Fang and R. O. Claus, "Polarization-independent all-fiber wavelength-division multiplexer based on a Sagnac interferometer", Opt. Lett., vol. 20, pp. 2146-2148, (1995).

[4] S. Li, K. S. Chiang, and W. A. "Gambling, Gain flattening of an erbium-doped fiber amplifier using a high-birefringence fiber loop mirror", IEEE Photon. Technol. Lett., vol. 13, pp. 942-944, (2001).

[5] L. Yuan, W. Jin, L. Zhou, Y. L. Hoo, M. S. Demokan, "Enhancement of multiplexing capability of low-coherence interferometric fiber sensor array by use of a loop topology", J. Lightwave Technol., Vol. 21, pp. 1313-1319, (2003).

[6] S. Yang, Z. Li, X. Dong, G. Kai, and Q. Zhao, "Generation of wavelength-switched optical pulse from a fiber ring laser with an F-P semiconductor modulator and a HiBi fiber loop mirror," IEEE Photon.Technol. Lett., vol. 14, pp. 774–776, (2002).

[7] N. Starodumov, L. A. Zenteno, D. Monzon, and E. De La Rose, "Fiber Sagnac interferometer temperature sensor," Appl. Phys. Lett. Vol. 70, pp. 19–21, (1997).

[8] S. Knudsen, A. B. Tveten, and A. Dandridge, "Measurements of fundamental thermal induced phase fluctuations in the fiber of a sagnac interferometer," IEEE Photon. Technol. Lett., vol. 7, pp. 90–92, (1995).

[9] E. De La Rose, L. A. Zenteno, A. N. Starodumov, and D. Monzon, "All-fiber absolute temperature sensor using an unbalanced high-birefringence Sagnac loop," Opt. Lett. vol. 22, pp. 481–483, (1997).

[10] Y. Liu, B. Liu, X. Feng, W. Zhang, G. Zhou, S. Yuan, G. Kai, and X. Dong, "High-birefringence fiber loop mirrors and their applications as sensors, " Appl. Opt., vol. 44, pp. 2382-2390, (2005).

[11] B. Dong, Q. Zhao, J. Lv, T. Guo, L. Xue, S. Li, and H. Gu, "Liquid-level sensor with a high-birefringence-fiber loop mirror, " Appl. Opt. , vol. 45, pp. 7767-7771, (2006).

[12] O. Frazão, B.V. Marquesa, P. Jorge, J.M. Baptista, J.L. Santos, "High birefringence D-type fibre loop mirror used as refractometer," Sensors and Actuators B: Chemical, vol. 135, pp. 108-111, (2008).

[13] O. Frazão, J.L. Santos, J.M. Baptista, "Simultaneous measurement for strain and temperature based on a long-period grating combined with a high-birefringence fiber loop mirror," IEEE Photon. Technol. Lett. vol. 18, pp. 2407-2409 (2006).

[14] G. Sun, D.S. Moon, Y. Chung, "Simultaneous temperature and strain measurement using two types of high-birefringence fibers in Sagnac loop mirror," IEEE Photon. Technol. Lett., vol. 19, pp. 2027-2029, (2007).

[15] O. Frazão, S. O. Silva, J. M. Baptista, J. L. Santos, G. Statkiewicz-Barabach, W. Urbanczyk, and J. Wojcik, "Simultaneous measurement of multiparameters using a Sagnac interferometer with polarization maintaining side-hole fiber" Appl. Opt. vol. 47, pp. 4841-4847, (2008).

[16] T. A. Birks, J. C. Knight, and P. S. J. Russell, "Endlessly single-mode photonic crystal fiber," Opt. Lett., vol. 22, pp. 961–963, (1997).

[17] P. St. J. Russell, "Photonic crystal fibers," Science, vol. 299, pp. 358–362, (2003).

[18] T. P. Hansen, J. Broeng, Stig E. B. Libori, E. Knudsen, A. Bjarklev, J. R. Jensen, and H. Simonsen, "highly birefringent index-guiding photonic crystal fibers", IEEE Photon. Technol. Lett., vol. 13, pp. 588-590, (2001).

[19] Ortigosa-Blanch, J. C. Knight, W. J. Wadsworth, J. arriaga, B. J. Mangan, T. A. Birks, and P. St. J. Russell, "Highly birefringent photonic crystal fibers", Optics Lett., vol. 25, pp. 1325-1327, (2000).

[20] K. Suzuki, H. Kubota, S. Kawanishi, H. Kubota, S. Kawanishi, "Optical properties of a low-loss polarization-maintaining photonic crystal fiber", Optics Express, vol. 9, pp. 676-680, (2001).

[21] C.-L. Zhao, X. Yang, C. Lu, W. Jin, M. S. Demokan, "Temperature- insensitive interferometer using a highly birefringent photonic crystal fiber loop mirror," IEEE Photon. Technol. Lett., vol. 16, pp. 2535-2537, (2004).

[22] D.-H. Kim, and J. U. Kang, "Sagnac loop interferometer based on polarization maintaining photonic crystal fiber with reduced temperature sensitivity," Opt. Express, vol. 12, pp. 4490–4495, (2004).

[23] Xiufeng Yang , Chun-Liu Zhao, Qizhen Peng, Xiaoqun Zhou, Chao Lu, "FBG sensor interrogation with high temperature insensitivity by using a HiBi-PCF Sagnac loop filter", Optics Communications, vol. 250，pp. 63-68 , (2005).

[24] X. Dong, H.Y. Tam, and P. Shum, "Temperature-insensitive strain sensor with polarization-maintaining photonic crystal fiber based Sagnac interferometer", Appl. Physics Lett., vol. 90, pp. 151113, (2007).

[25] O. Frazão, J. M. Baptista, and J. L. Santos, "Temperature-independent strain sensor based on a Hi-Bi photonic crystal fiber loop mirror," IEEE Sens. J. vol. 7, pp. 1453–1455, (2007).

[26] O. Frazão, J. M. Baptista, J. L. Santos, and P. Roy, "Curvature sensor using a highly birefringent photonic crystal fiber with two asymmetric hole regions in a Sagnac interferometer," Appl. Opt. vol. 47, pp. 2520–2523, (2008).

[27] G. Kim, T. Cho, K. Hwang, K. Lee, K. S. Lee, Y.-G. Han, and S. B. Lee, "Strain and temperature sensitivities of an elliptical hollow-core photonic bandgap fiber based on Sagnac interferometer," Opt. Express, vol. 17, pp. 2481–2486, (2009).

[28] H. M. Kim, T. H. Kim, B. Kim, and Y. Chung, "Temperature-insensitive torsion sensor with enhanced sensitivity by use of a highly birefringent photonic crystal fiber," IEEE Photonics Technology Letters, vol. 22, pp.1539-1541, (2010).

[29] H.Y. Fu, H.Y. Tam, L.-Y. Shao, X. Dong, P.K.A. Wai, C. Lu, and Sunil K. Khijwania, "Pressure sensor realized with polarization-maintaining photonic crystal fiber-based Sagnac interferometer", Appl. Opt., vol. 47, pp. 2835-1839, (2008).

[30] H. Gong, C. C. Chan, L. Chen, and X. Dong, "Strain sensor realized by using low-birefringence photonic-crystal-fiber-based Sagnac loop", IEEE Photon. Technol. Lett., vol. 22, pp. 1238-1240, (2010).

[31] H. Gong, C. C. Chan, P. Zu, L. Chen, and X. Dong, "Curvature measurement by using low-birefringence photonic crystal fiber based Sagnac loop", Opt. commun., vol. 283, pp. 3142-3144, (2010).

[32] P. Zu, C. C. Chan, Yongxing Jin, Tianxun Gong, Yifan Zhang, Li Han Chen and Xinyong Dong "A temperature-insensitive twist sensor by using low-birefringence photonic crystal fiber based sagnac interferometer", IEEE Photonics Technology Letters, vol. 25, pp. 1041-1135, (2011).

[33] W. Qian, C.-L. Zhao, S. He, X. Dong, S. Zhang, Z. Zhang, S. Jin, J. Guo and H. Wei, "High-sensitivity temperature sensor based on an alcohol-filled photonic crystal fiber loop mirror", Opt. Lett., vol. 36, pp. 1548-1550, (2011).

[34] W. Qian, C.-L. Zhao, X. Dong, and W. Jin, "Temperature independent strain sensor based on intensity measurement using a highly birefringent photonic crystal fiber loop mirror," Opt. commun., vol. 283, pp. 5250-5254, (2010).

[35] H. Y. Fu, A. C. L. Wong, P. A. Childs, H. Y. Tam, Y. B. Liao, C. Lu, and P. K. A. Wai, "Multiplexing of polarization-maintaining photonic crystal fiber based Sagnac interferometric sensors", Optics Express, vol. 17, pp. 18501-18512, (2009).

[36] Bertholds and R. Dandliker, "Determination of the individual strain-optic coefficients in single-mode optical fibres", J. Lightwave Technol. vol. 6, pp. 17-20, (1988).

[37] D. Kersey, M. A. Davis, H. J. Patrick, M. LeBlanc, K. P. Koo, C. G. Askins, M. A. Putnam, and E. J. Friebele, "Fiber grating sensors", J. Lightwave Technol. vol. 15, pp. 1442-1463, (1997).

[38] Y. Zhang, D. Feng, Z. Liu, Z. Guo, X. Dong, K. S. Chiang, and B.C. B. Chu, "High-sensitivity pressure sensor using a shielded polymer-coated fiber Bragg grating," IEEE Photon. Technol. Lett. vol. 13, pp. 618–619 (2001).

[39] H. K. Gahir and D. Khanna, "Design and development of a temperature-compensated fiber optic polarimetric pressure sensor based on photonic crystal fiber at 1550 nm," Appl. Opt. vol. 46, pp. 1184–1189 (2007).

[40] Y. Yu, X. Li, X. Hong, Y. Deng, K. Song, Y. Geng, H. Wei, and W. Tong, "Some features of the photonic crystal fiber temperature sensor with liquid ethanol filling", Opt. Express, vol. 18, pp. 15383-15388, (2010).

[41] L. Liu, Q. Zhao, G. Zhou, H. Zhang, S. Chen, L. Zhao, Y. Yao, P. Guo, and X. Dong, "Study on an optical filter constituted by concatenated Hi-Bi fiber loop mirrors," Microw. Opt. Technol. Lett. vol. 43, pp. 23–26, (2004).

[42] O. Frazão, J. L. Santos, and J. M. Baptista, "Strain and temperature discrimination using concatenated high-birefringence fiber loop mirrors," IEEE Photon. Technol. Lett. vol. 19, pp. 1260–1262, (2007).

[43] C. L. Wong, P. A. Childs, and G. D. Peng, "Multiplexed fibre Fizeau interferometer and fibre Bragg grating sensor system for simultaneous measurement of quasi-static strain and temperature using discrete wavelet transform," Meas. Sci. Technol. vol. 17, pp. 384–392, (2006).

[44] P. A. Childs, "An FBG sensing system utilizing both WDM and a novel harmonic division scheme," J. Lightwave Technol. vol. 23, pp. 348–354, (2005), "Erratum" 23, 931 (2005).

Recent Progress in Optical Fiber Research

Edited by Dr Moh. Yasin

ISBN 978-953-307-823-6

Hard cover, 450 pages

Publisher InTech

Published online 25, January, 2012

Published in print edition January, 2012

This book presents a comprehensive account of the recent progress in optical fiber research. It consists of four sections with 20 chapters covering the topics of nonlinear and polarisation effects in optical fibers, photonic crystal fibers and new applications for optical fibers. Section 1 reviews nonlinear effects in optical fibers in terms of theoretical analysis, experiments and applications. Section 2 presents polarization mode dispersion, chromatic dispersion and polarization dependent losses in optical fibers, fiber birefringence effects and spun fibers. Section 3 and 4 cover the topics of photonic crystal fibers and a new trend of optical fiber applications. Edited by three scientists with wide knowledge and experience in the field of fiber optics and photonics, the book brings together leading academics and practitioners in a comprehensive and incisive treatment of the subject. This is an essential point of reference for researchers working and teaching in optical fiber technologies, and for industrial users who need to be aware of current developments in optical fiber research areas.

InTech Europe
University Campus STeP Ri
Slavka Krautzeka 83/A
51000 Rijeka, Croatia
Phone: +385 (51) 770 447
Fax: +385 (51) 686 166
www.intechopen.com

InTech China
Unit 405, Office Block, Hotel Equatorial Shanghai
No.65, Yan An Road (West), Shanghai, 200040, China
中国上海市延安西路65号上海国际贵都大饭店办公楼405单元
Phone: +86-21-62489820
Fax: +86-21-62489821

IntechOpen